Journal of Geophysical Research: Earth Surface

RESEARCH ARTICLE
10.1002/2017JF004461

This article is a companion to Pelletier (2018) https://doi.org/10.1002/2017JF004462, Barchyn (2018) https://doi.org/10.1002/2018JF004629.

Key Points:
- Yardang morphology at the study site is controlled by bedrock structure
- Sediment flux is near saltation-suspension transition and highest in troughs
- Erosion rates are several mm/yr over time scales of ~10^0 and ~10^6 years

Supporting Information:
- Supporting Information S1
- Table S1
- Table S2
- Table S3
- Table S4

Correspondence to:
J. D. Pelletier,
jdpellet@email.arizona.edu

Citation:
Pelletier, J. D., Kapp, P. A., Abell, J., Field, J. P., Williams, Z. C., & Dorsey, R. J. (2018). Controls on yardang development and morphology: 1. Field observations and measurements at Ocotillo Wells, California. *Journal of Geophysical Research: Earth Surface*, *123*, 694–722. https://doi.org/10.1002/2017JF004461

Received 14 AUG 2017
Accepted 3 FEB 2018
Accepted article online 2 APR 2018
Published online 26 APR 2018

Controls on Yardang Development and Morphology: 1. Field Observations and Measurements at Ocotillo Wells, California

Jon D. Pelletier[1], Paul A. Kapp[1], Jordan Abell[2,3], Jason P. Field[1], Zachary C. Williams[1], and Rebecca J. Dorsey[4]

[1]Department of Geosciences, University of Arizona, Tucson, AZ, USA, [2]Department of Earth and Environmental Sciences, Columbia University, New York, NY, USA, [3]Lamont-Doherty Earth Observatory, Columbia University, Palisades, NY, USA, [4]Department of Geological Sciences, University of Oregon, Eugene, OR, USA

Abstract Yardangs are streamlined hills formed in part by the erosive action of wind and wind-blown sediments. Here we examine the controls on yardang development and morphology using the Ocotillo Wells State Vehicular Recreation Area (OWSVRA), California, as a study site. We measured the compressive strengths, strikes, and dips of bedrock strata, eolian sediment fluxes (including their vertical profiles and spatial variations around yardangs), and erosion rates derived from geologic constraints and multitemporal Terrestrial Laser Scanning (TLS). We used a combination of TLS-based and airborne lidar-based Digital Elevation Models (DEMs) to test the applicability of an asymmetric Gaussian function for characterizing yardang form and quantify the relationships among yardang lengths, widths, heights, spacings, and their controlling factors. Yardang aspect ratios are controlled by bedrock structural attributes, specifically by the tangent of the dip and the angle between the strike and the prevailing wind direction. Yardang spacings scale linearly with yardang width. Yardang heights increase as the square root of width such that larger yardangs tend to have gentler side slopes. Sediment fluxes reach a maximum in the troughs among yardangs, consistent with the hypothesis that yardang development involves the focusing of wind and wind-blown sediments into troughs. The vertical distribution of eolian sediment flux follows a power law with an exponent of −2.5, a result consistent with an advection-diffusion-settling model of transport near the saltation-suspension transition. Erosion rates are several mm/yr over time scales of ~10^0 and ~10^6 years.

1. Introduction

1.1. Problem Statement

Yardangs are streamlined ridges, carved into bedrock or cohesive sediments, that form parallel to the prevailing wind direction. Yardangs are commonly asymmetric in shape with blunt windward sides characterized by steep, often near-vertical slopes, and lee sides that gradually decline in elevation and taper to a point (Blackwelder, 1934; Bosworth, 1922; Breed et al., 1989; El-Baz et al., 1979; Goudie et al., 1999; Hedin, 1905; McCauley et al., 1977). Yardangs form in many arid regions on Earth and on Mars and Venus (Greeley et al., 1995; Greeley & Iversen, 1985; Ward, 1979; Ward & Greeley, 1984). Yardangs serve as paleoclimatic indicators because they record the prevailing wind direction over the time scale of their formation, that is, typically ~10^3–10^5 years (Laity, 2011; Laity & Bridges, 2009).

Yardang development involves positive feedbacks among topography, spatial variations in near-surface wind speeds, eolian sediment fluxes, and erosion rates. In the prevailing conceptual model for yardang development, troughs among yardangs are initiated at preexisting fluvial channels and/or weaknesses in the substrate (Blackwelder, 1934). Wind and wind-blown sediments are then focused into the incipient troughs, leading to further deepening and the accommodation of wind and wind-blown sediment in a positive feedback (Halimov & Fezer, 1989). Yardang development can involve both eolian and noneolian processes, as mass wasting and fluvial erosion can be important contributors to yardang erosion (Brookes, 2001; Laity, 2011).

This conceptual model is well supported by previous studies, but basic questions remain regarding how yardangs develop and what variables control their morphology. For example, the hypothesis that the troughs among yardangs are initiated in preexisting channels and/or fractures suggests that the periodicity of yardangs may be primarily related to the periodicity of those initial channels and/or fractures. Trough deepening, however, may also involve an instability that is initiated at small-scale, aperiodic microtopographic lows,

and/or substrate weaknesses. In such cases the resulting periodicity may be controlled primarily by the spatial scale at which the focusing of wind and wind-blown sediment into incipient troughs is maximized. These hypotheses are not mutually exclusive: yardang formation may be primarily related to periodic preexisting features in some cases and a scale-selective instability in other cases. In this paper we present field observations aimed at testing these and other hypotheses related to yardang development.

In the most widely cited study of yardangs to date, Ward and Greeley (1984) argued that yardangs evolve to an ideal length-to-width (i.e., aspect) ratio of 4 because this ratio minimizes the sum of pressure drag and skin-friction drag. Similar minimum-drag concepts have been applied to subaqueous streamlined bedforms (e.g., Komar, 1983, 1984). Yardang aspect ratios on Earth (de Silva et al., 2010; Dong et al., 2012; Hu et al., 2017) and Mars (Mandt et al., 2008) vary by 2 orders of magnitude (i.e., 2–200), however, suggesting that the minimum-drag model of Ward and Greeley (1984) requires further assessment. Evidence suggests that yardang aspect ratios may, in some cases, be controlled primarily by characteristics (e.g., the strikes, dips, and stratal thicknesses) of the substrate. Brookes (2003), for example, studied yardangs cut into exhumed meander scrolls in a region of unidirectional winds. He documented larger aspect ratios where yardangs developed parallel to the long axis of the scrolls and smaller aspect ratios where the wind was perpendicular. Hu et al. (2017) documented lower mean aspect ratios on the windward sides of anticlines relative to the leeward sides in the Qaidam Basin of northwestern China. However, we lack a quantitative and theoretical understanding of how yardang morphology relates to specific measures of substrate heterogeneity, such as the strike and dip angles of the strata and/or the difference in compressive strengths among strong and weak strata.

This paper describes observations and measurements aimed at developing a better quantitative understanding of the relationships among processes and form in yardangs using the yardangs of the Ocotillo Wells State Vehicular Recreation Area (OWSVRA) as type examples. The primary goals of this work are to (1) provide a geologic framework for understanding the development of yardangs in the OWSVRA; (2) measure and compare erosion rates in the study area over both short (~10^0 years) and long (~10^6 years) time scales and use those data to constrain the topographic diffusivity associated with water-driven erosional processes that play an important role in driving erosion on the tops and lee sides of yardangs; (3) characterize the mechanical properties of the substrate within which yardangs develop, including strikes, dips, and the mean and variability of compressive strengths of strata; (4) quantify the vertical profiles of wind and wind-blown sediments in both unperturbed locations upwind from yardangs and in yardang troughs where wind and sediment have been hypothesized to be focused; (5) test the applicability of the asymmetric Gaussian function for characterizing yardang form; and (6) quantify the relationships among yardang lengths, widths, heights, and spacings, and their controlling factors.

In the companion paper (Pelletier, 2018) we demonstrate that an asymmetric Gaussian topography is consistent with a yardang evolving primarily via water-driven processes on its top and lee sides coupled with a pattern of eolian abrasion that is consistent with data on the spatial distribution of sediment flux presented in this paper. More broadly, the observations and data described in this paper form the basis for a numerical model of yardang formation described in the companion paper (Pelletier, 2018).

1.2. Study Site

1.2.1. Introduction

The most well-studied yardang field in North America is on the northeast side of Rogers Lake, California (Blackwelder, 1934; Ward & Greeley, 1984). Rogers Lake has two key limitations. First, few of the yardangs at Rogers Lake are isolated landforms. The majority of yardangs at Rogers Lake grade upslope into rolling hills of shoreline deposits (Ward & Greeley, 1984). As a result, the Rogers Lake yardangs have compound shapes that make it difficult to clearly identify the boundaries of individual yardangs and the controls on their form. Second, the Rogers Lake yardangs are composed of flat-lying consolidated sediments, making it difficult to determine how variations in substrate structure might affect yardang morphology. In contrast, OWSVRA has many isolated yardangs with ideal forms, sculpted from sedimentary rock that has been deformed into anticlinoria and synclinoria with wavelengths ranging from ~100 to 800 m, providing a range of strikes and dips that allow the hypothesis of structural control on yardang morphology to be tested. To our knowledge, the yardangs of OWSVRA have not previously been described in the scientific literature.

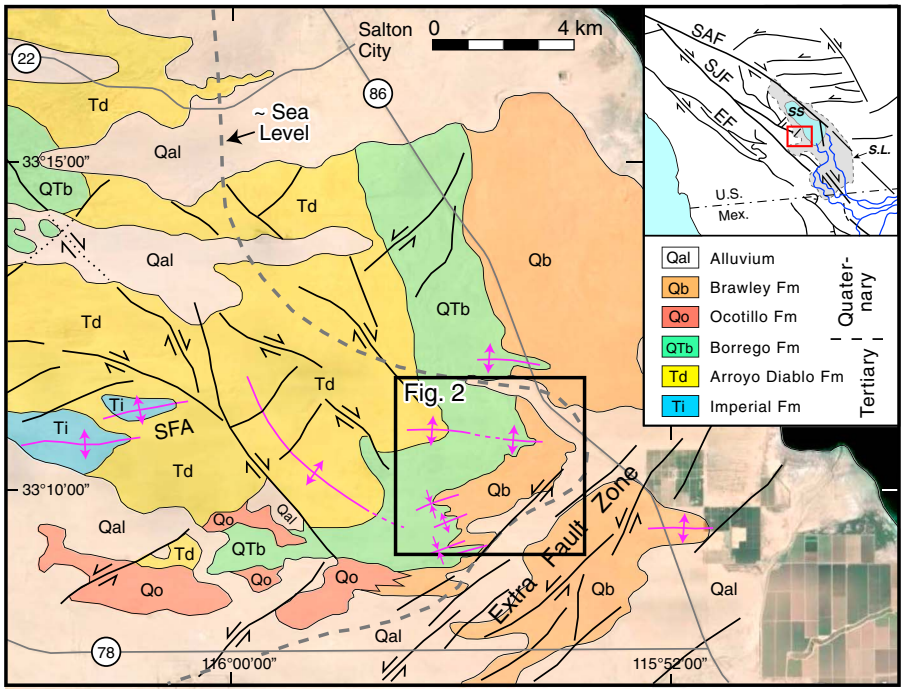

Figure 1. Geologic map of the San Felipe Hills, west of the Salton Sea, southern California (red box in inset shows location). Modified from Janecke et al. (2010) and Kirby et al. (2007). Abbreviations: EF, Elsinore Fault; SAF, San Andreas Fault; SFA, San Felipe anticline; SJF, San Jacinto Fault; S.L., sea level; SS, Salton Sea.

Streamlined hills oriented parallel to the predominant WSW wind direction occur throughout the southeastern portion of OWSVRA identified in Figure 1a and in greater detail in Figure 2. However, there are two areas where isolated yardangs are particularly abundant. We focused our field observations and measurements in those areas (Figures 3b and 3c).

Although OWSVRA allows off-road vehicle use, travel is restricted to established trails that generally coincide with large fluvial channels (i.e., those with drainage areas larger than ~10 km^2). The loose, friable nature of the soil on the lee sides of yardangs preserves footprints for more than a year. During the 2013–2015 period when we performed our field work, we observed no signs of vehicle traffic, and only our own foot traffic (limited to a narrow path along the tops of yardangs) on the yardangs we studied. As such, we are confident that the impact of recreation in some portions of the park did not compromise any aspect of our study.

1.2.2. Geology

The study area exposes mud-dominated lacustrine strata of the Pliocene-Pleistocene Borrego Formation and unconformably overlying, generally coarser-grained fluvial-deltaic-lacustrine strata of the lower Pleistocene Brawley Formation (Figures 1 and 2; Janecke et al., 2010; Kirby et al., 2007). These strata are variably deformed into broad-plunging to tightplunging, mostly east to ENE plunging folds. The axial traces of the folds are oriented ~45–80° from the major NW striking dextral strike-slip faults of the southern San Andreas fault system, consistent with a dextral wrench tectonic setting. Dextral transpressional deformation initiated in OWSVRA ca. 1.1–1.3 Ma during initiation of the San Jacinto and related strike-slip fault zones west of the Salton Sea (Janecke et al., 2010). Neotectonic deformation is evidenced by locally steep dips and tight folds in the equivalent Ocotillo and Brawley Formations, which are ~1.1–0.5 Ma (Kirby et al., 2007; Lutz et al., 2006). The zero elevation contour (sea level) wraps around the eastern end of the study area, around the core of a major anticlinorium (Figure 1), providing evidence for post-0.5 Ma uplift in this structural culmination. The youngest strandline of Pleistocene Lake Cahuilla (Waters, 1983) similarly follows topographic contours west of the modern Salton Sea, reflecting the active-tectonic control on modern topography and landforms in this area.

An appreciation of the geologic framework of the study area is important for understanding the development of OWSVRA yardangs in two ways. First, the fact that yardangs are generally restricted to the most

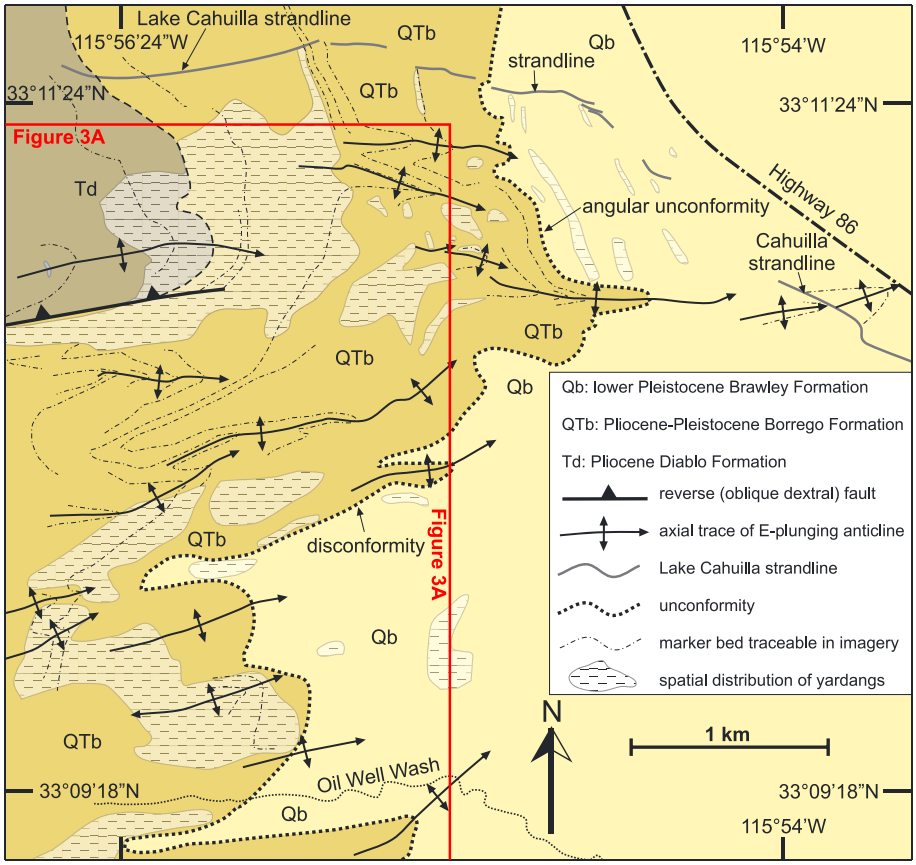

Figure 2. Simplified geologic map of the study area.

structurally heterogeneous rock formation in OWSVRA (the Borrego Formation) suggests that yardang development is enhanced by substrate heterogeneity. Second, the well-constrained thickness and age of the Borrego Formation (Housen and Dorsey, 2010) and the Pleistocene structural-stratigraphic history (Janecke et al., 2010; Kirby et al., 2007; Lutz et al., 2006) permit an estimate of the erosion rate over geologic time scales against which short-term erosion rates measured by multitemporal TLS can be compared. Knowledge of the erosion rate, together with an analysis of the topographic curvature on the tops and lee sides of yardangs, enables the topographic diffusivity (which quantifies the efficiency of erosion by water-driven processes) to be estimated. The tops and lee sides of yardangs are heavily influenced by water-driven processes due to the limited eolian sediment flux available to drive abrasion at heights ≈1 m above the ground and on the lee sides of yardangs.

Although yardangs are locally present in the Brawley Formation, they are more abundant and widespread within the generally finer-grained and more heterogeneous Borrego Formation, which consists of friable red laminated-to-massive claystone, mudstone, and siltstone with lesser, more erosionally resistant sandstone and marlstone. Sandstone beds in the Borrego Formation are up to 4-m thick and are composed dominantly of sublitharenite derived from the Colorado River. The east plunging nature of the folds results in an overall dominant bedding dip direction toward the east. Rows of yardangs are most prominent where the strata strike subperpendicular to, and dip in the same direction as, the prevailing wind direction. It is also notable that rows of yardangs terminate abruptly to the north at, and on the topographically higher side, of the Lake Cahuilla strandlines (Figure 2). This suggests that active rock uplift in the core of the east plunging anticlinorium may play a significant role in promoting yardang development. In the absence of active uplift, the troughs among yardangs cannot undergo persistent downcutting, potentially limiting yardang development or promoting yardang demise. Alternatively, it is possible that wave-cut erosion associated with Lake Cahuilla could have beveled yardangs that existed below the level of the strandlines.

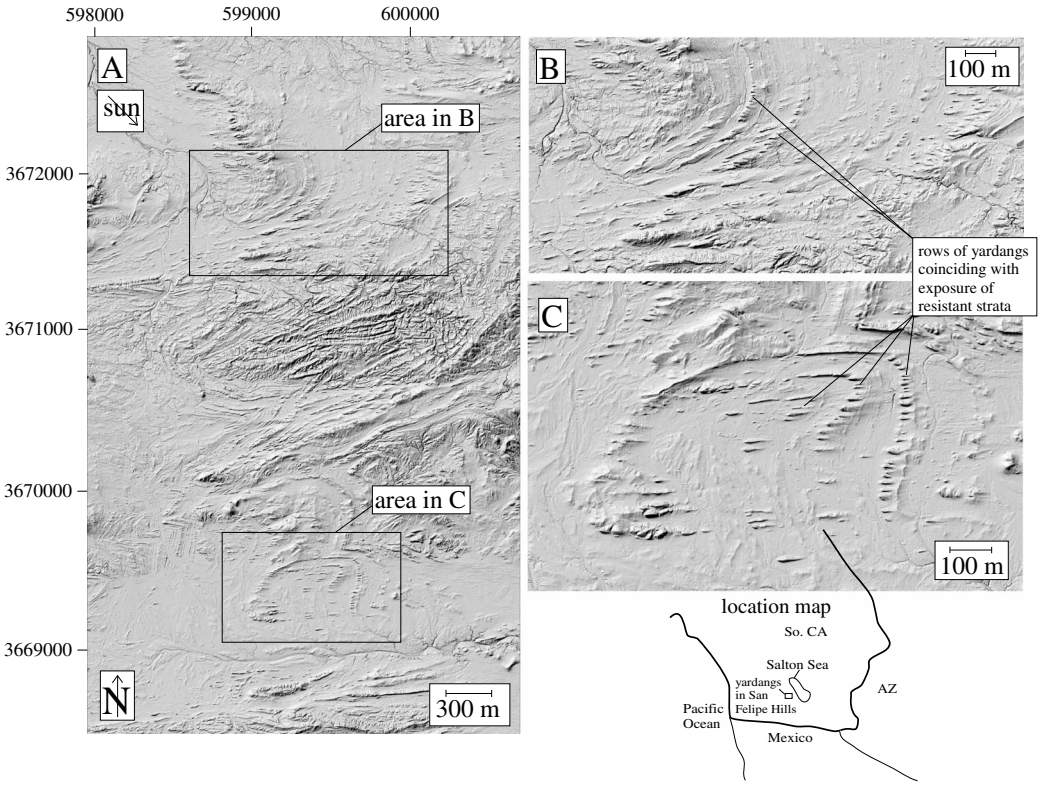

Figure 3. Shaded-relief images of the principal yardang fields in Ocotillo Wells State Vehicular Recreation Area (OWSVRA).

In and near the study area, the Borrego Formation is up to 1.8-km thick (Housen and Dorsey, 2010) and the overlying Brawley Formation is a minimum of 500-m thick (Kirby et al., 2007). The depositional base of the Borrego Formation, and its contact with the underlying Arroyo Diablo Formation, is located ≈500 m west of the study area. Using the stratigraphic thickness of units combined with knowledge of the Pleistocene deformation history in the western Salton Trough, we can estimate the erosion rate over geologic time scales. The Borrego Formation is estimated from map data to be ≈800–1,200-m thick in the study area (Figure 2). The upper part of the Arroyo Diablo Formation in the northwest part of Figure 2 is ≈200–300-m thick, and the Brawley Formation is ≈500-m thick (Kirby et al., 2007). We therefore estimate that ≈1.5–2.0 km of strata have been eroded from the structurally deepest core of the OWSVRA anticlinorium during the past ca. 500 kyr (end of deposition of the Brawley Formation). This yields an approximate erosion rate of 3–4 m/kyr, fast considering the arid climate and low relief (tens of meters over horizontal scales ~1 km), but consistent with the relatively soft, friable nature of the rocks. The total amount and rate of erosion decrease away from the core of the main anticlinorium in the northwest corner of Figure 2.

A second estimate of erosion rate can be determined based on exposure of the Imperial Formation in the core of the San Felipe anticline west of the study area (Figure 1). We estimate ca. 200–400 m of upper Imperial Formation exposed in the core of the anticline (assuming 20–30° average dip). The Arroyo Diablo Formation is ≈2.5-km thick in the Fish Creek-Vallecito basin (Dorsey et al., 2011), although its thickness is not well known in the San Felipe Hills and could be somewhat less there. As the overlying Borrego Formation is ≈1.7–1.8-km thick in the Borrego Badlands (Housen and Dorsey, 2010) and ≈0.8–1.2 km in the study area, we assume an intermediate thickness of ≈1.4 km in the western part of Figure 1. The angular unconformity at the top of the Borrego Formation and the age of that contact (1.1 Ma) (Kirby et al., 2007; Lutz et al., 2006) indicate that transpressional deformation and uplift began ca. 1.1 Ma. The total thickness eroded from the core of the San Felipe anticline (3.5–4.3 km) thus yields an average erosion rate of ≈3–4 mm/yr since 1.1 Ma, similar to the rate calculated since 0.5 Ma. The erosion rate estimates described in this section are used in section 3.3.3 to infer the topographic diffusivity associated with the water-driven erosional processes that are an important driver of erosion on the tops and lee sides of yardangs.

1.2.3. Climate, Vegetation, and Winds

The climate of OWSVRA is arid and hot, with mean annual precipitation of approximately 6 cm and average daily high temperatures of between 21 °C in December and January to 43 °C in July (Western Regional Climate Center (WRCC), 2016a). Approximately 75% of the annual rainfall occurs during the cold-season months from October to March, primarily as low- to moderate-intensity frontal storms. Brief, high-intensity thunderstorms can occur from July to September when approximately 20% of the annual rainfall is recorded. Rills are pervasive on the tops and lee sides of yardangs, indicating that runoff that drives erosion occurs episodically on yardangs.

Vegetation in the southeastern portion of OWSVRA is extremely sparse and composed almost exclusively of creosote (*Larrea tridentate*) approximately 2 m or less in height. In 2014 we counted fewer than 100 creosote individuals in the ~0.3-km^2 area composing the central portion of Figure 3c. None of the yardangs have any vegetation cover whatsoever.

Two nearby weather stations provide historical data for wind speeds and directions: CWOP station DW1021, located in Borrego Springs 30 km WNW of the study area, and CIMIS station Salton Sea East, located 30 km ENE of the study area. CWOP station DW1021 provides data for mean wind speeds and directions at 15-min intervals for 2009–2015 (University of Utah, 2016), and the CIMIS station provides mean hourly wind data for 1995–2012 (Western Regional Climate Center (WRCC), 2016b). There is a third station (CIMIS Salton Sea West) that is closer to the study site than the two stations considered here, but data from that station (Western Regional Climate Center (WRCC), 2016c) appear to be unrepresentative of regional patterns since they record primarily northwesterly winds, which is inconsistent with the orientation and migration direction of barchans (Pelletier, 2013) located close to both the CIMIS Salton Sea West and the yardang fields considered in this paper.

Data from CWOP DW1021 (measurement height of 10 m) and CIMIS Salton Sea East (measurement height of 2 m) are consistent regarding the directions and speeds of the fastest winds, which come primarily from the W and WSW (Figures 4a and 4b). Winds from the E and ESE are also common but are almost always slower than 5 m/s. Winds from the W and WSW exceed 15 m/s for approximately 24 hr every year (0.25% of the time). The predominant WSW direction of the fastest winds is consistent with orientations of the yardangs, which have an average upwind orientation of 265° (5°S of west) where larger-scale topographic obstacles are not present.

1.2.4. Process Observations and Conceptual Model for Yardang Development

The area of Figure 3c is a doubly plunging anticline within which yardangs tend to have formed in rows that follow structural contours (Figures 3c and 5a). We observed an exposed sandstone unit with a compressive strength of at least 5 MPa (see section 3.1 for data) on the windward side of every yardang in the study area. These resistant strata most commonly outcrop at or just below the inflection point in the topographic cross section. In Figure 5b, for example, the windward side of the yardang has an upper portion that is relatively fine-grained, mechanically weak, pervasively rilled, and convex (i.e., the topography has a negative Laplacian) and a lower portion that is mechanically stronger, generally lacking in soil cover and rills, and straight or concave. The resistant sandstone bed coincides with the transition from these two portions of the topographic cross section. As such, field observations at OWSVRA corroborate the hypothesis that yardang formation is initiated or enhanced by the exposure of resistant strata on the windward sides of yardangs.

The lowest approximately 1 m of the troughs among yardangs exhibit evidence for eolian abrasion, including facets sloping into the wind and wind-aligned pits, flutes, and grooves (Figures 5c and 5d). Abrasional erosion of the troughs among yardangs is intermittent over time scales of ~10 years since sand sheets move through the troughs, temporarily protecting the troughs from abrasion (see section 3.4 for details of the multitemporal TLS surveys that document sand sheet migration through the troughs).

The windward sides of yardangs also exhibit evidence for bedrock weathering (fracturing of relatively resistant layers by freeze-thaw and/or other physical weathering processes common to most hillslopes) and subsequent rockfall (Figure 5b; Al-Dousari et al., 2009; Hörner, 1932; Krinsley, 1970; Laity, 2011). These processes may be accelerated by the abrasional undercutting of the more resistant sandstone layers. Rockfall debris transported to the base of the slope can then be abraded or weathered into sediments that can be entrained by the wind.

The upper portions of the windward sides of yardangs and the entire lee sides of yardangs at OWSVRA are soil-mantled and pervasively rilled (Figure 5a). The absence of vegetation and the relatively fine-grained

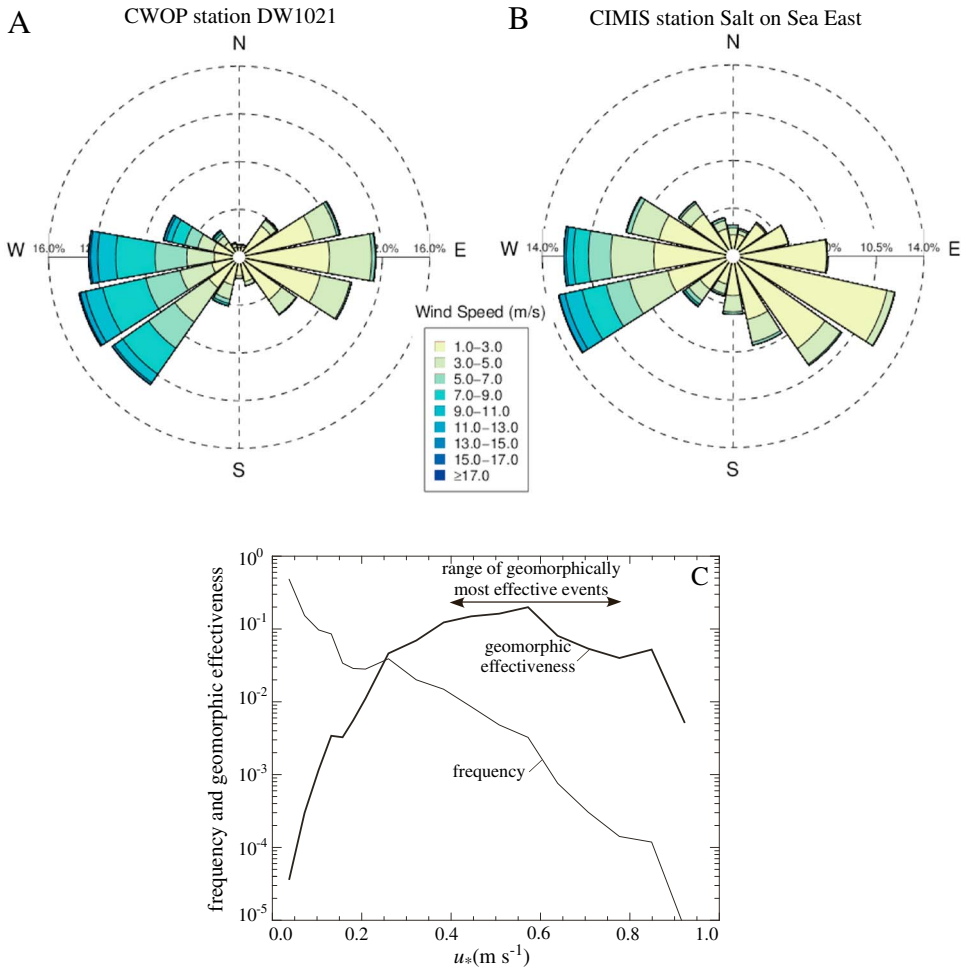

Figure 4. (a and b) Wind rose diagrams from the two nearby wind measurement stations. Left: CWOP station DW1021. Right: CIMIS station Salton Sea East. (c) Plots illustrating the calculation of the geomorphically most effective shear velocity. The thin curve represents the distribution of shear velocities measured at CWOP DW1021. The thick line is the distribution multiplied by the geomorphic work associated with each shear velocity, which increases as the fourth power of shear velocity. The resulting curve suggests that the geomorphically most effective wind storms are associated with shear velocities in the range of 0.4 to 0.8 m/s.

nature of the siltstone and mudstone that dominates both the Borrego Formation and the lee sides of yardangs in OWSVRA suggest that interrill and rill erosion; that is, rain splash detachment of particles and subsequent transport by overland and rill flow, are important and potentially dominant processes on the tops and lee sides of yardangs. Deflation, that is, removal of loose material by the wind, may also be an important process, but this hypothesis is difficult to evaluate based on field observations alone, in part because deflation lacks a microtopographic signature.

Figure 5e illustrates a conceptual model of yardang formation based on field observations at OWSVRA. Troughs are lowered by the deflection of wind and wind-blown sediments around resistant layers exposed on the windward sides of yardangs. The heterogeneity of the substrate is characterized by the mechanical strengths, thicknesses, and strikes and dips of bedrock strata. The lowest ≈1 m of the yardang troughs and windward sides are eroded primarily by eolian abrasion. The lowest portions of windward sides are also susceptible to bedrock weathering and rockfall, perhaps accelerated by undercutting of resistant strata by eolian abrasion of less resistant beds. Eolian abrasion of the lower portions of the windward sides of yardangs and the troughs among yardangs is intermittent, as sand waves move through the area with rates ~10 m/yr and temporarily cover the troughs. Above ≈1 m in height, erosion by water-dominated processes is an important process in combination with occasional abrasion by windstorms sufficiently intense to drive significant sediment transport at such heights. This conceptual model suggests that a better understanding of the relationships among processes and form in yardangs requires measurements of the spatial variability

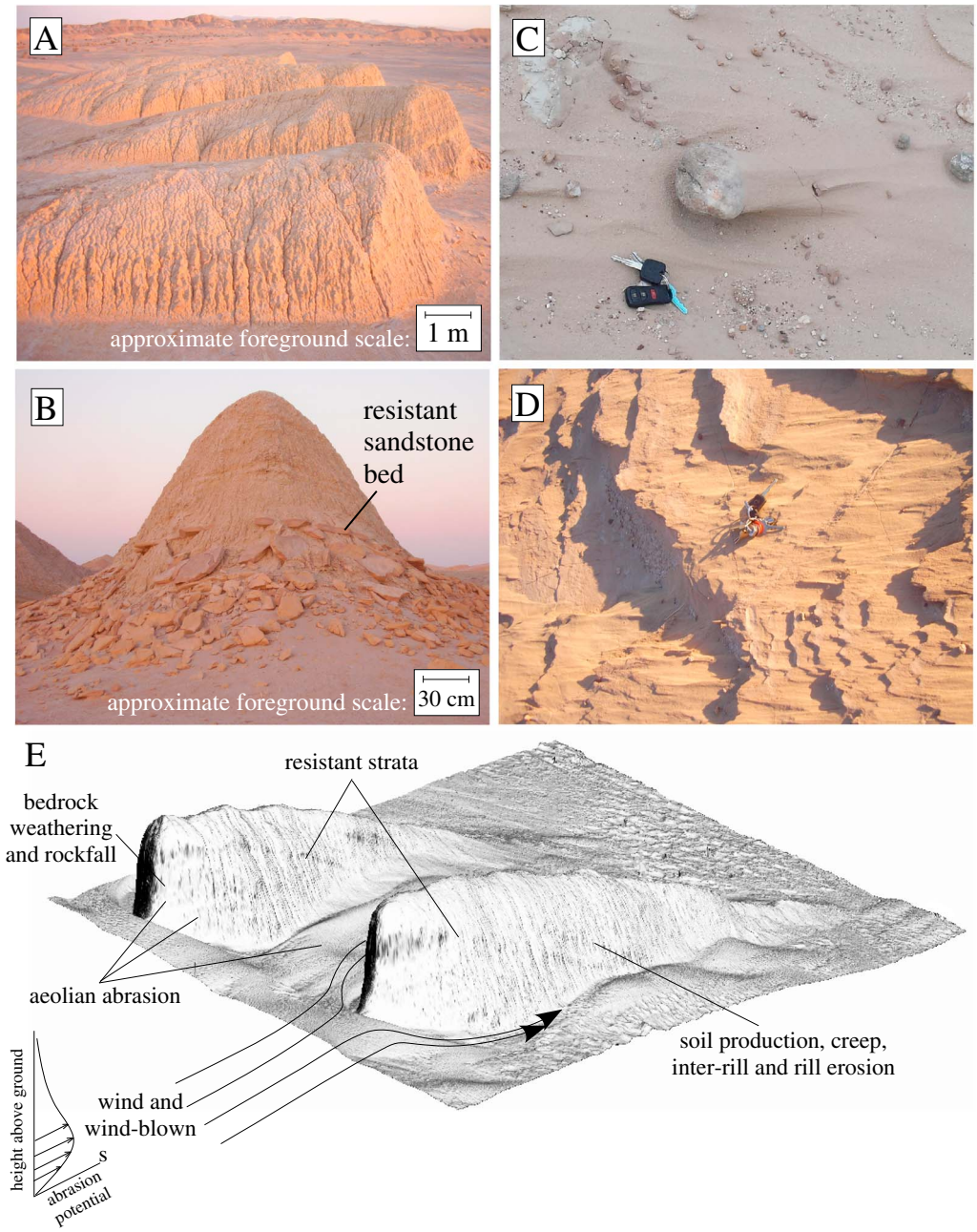

Figure 5. Photographs documenting key field observations. (a) The lee sides of yardangs in OWSVRA are soil-mantled and pervasively rilled. (b) Resistant beds form small cliffs and overhangs on the windward sides of yardangs. (c and d) Ventifacts and similar signatures of abrasion are common in the troughs between yardangs where sand has not backfilled the troughs. (e) Diagram illustrating principal processes controlling yardang development.

of eolian sediment fluxes, erosion rates, and the structure (i.e., strikes, dips, and variability of mechanical strength) of the substrate. These measurements, and their interpretations, are the focus of the remainder of the paper.

2. Methods

2.1. Structural Data

The strikes and dips of resistant sandstone beds exposed on the windward sides of approximately 100 yardangs were measured with a Brunton compass Table S1 (supporting information). Two to three individual measurements were averaged to obtain a representative value for each yardang. The compressive

strengths of these beds were measured with a Schmidt Hammer (SilverSchmidt model). The mudstones and siltstones were not sufficiently strong to exceed the minimum value of 5 MPa measurable with the Schmidt Hammer in any of the yardangs we measured. As such, the compressive strengths we measured are not a uniform or equal sampling of all sedimentary strata but instead represent the strengths of only the more resistant sandstone beds within the Borrego Formation. Compressive strength is relevant to this study because the resistance of solids to abrasion increases with compressive strength (e.g., Witte & Backstrom, 1951).

The Schmidt Hammer records a Q value by measuring the rebound of a spring-loaded mass. This value was converted to a compressive strength σ (in MPa) using the calibration equation for the specific model of Schmidt Hammer we used:

$$\sigma = c_1 e^{c_2 Q} \tag{1}$$

where $c_1 = 2.77$ and $c_2 = 0.048$.

2.2. Measurement and Analysis of Eolian Sediment Fluxes and Grain Size

Sediment fluxes were measured at four logarithmically spaced heights above the ground (0.09, 0.21, 0.42, and 1.02 m) at eight locations around two pairs of yardangs over five time intervals using Modified Wilson and Cooke (MWAC) sediment samplers (Wilson & Cooke, 1980). The goal of this work was to quantify the spatial variability in sediment flux as a means of inferring spatial variations in abrasion rate. The MWAC samplers we used have a ½-inch diameter PVC tube inlet that collects sediment in a high-density polyethylene bottle capable of storing approximately 1 kg of sediment without impeding wind flow into the bottle. A similar tube bending in the opposite directions returns air at the downwind side of the bottle. Each MWAC was positioned so that the inlet was oriented in the direction of the prevailing wind. Four MWACS were mounted to each of eight towers constructed of welded pieces of electrical strut that hold each of the four MWACs firmly in place.

The set of eight MWAC towers, each with four MWACS, was deployed at five time intervals between May and June 2015, ranging in length from 1 hr (during the peak of a wind storm event) to 12 days (1: 14 May 2015 from 5:30 to 6:30 pm, 2: 14 May 7:30 pm to 16 May, 3: 16–21 May 4: 21–24 May, and 5: 24 May to 4 June), for a total of $4 \times 8 \times 5$ measurements of eolian sediment flux. The time intervals used for measurement were necessarily shorter during faster wind conditions because the MWACS have a limited storage capacity. The bottles were emptied at the end of each measurement interval, and the sediments were weighed. The MWAC towers were deployed around two pairs of yardangs, one with no sediment stored in the trough between the yardangs (i.e., a locally supply-limited case) and the other with sediment stored in the trough (a locally transport-limited case) in order to test whether the vertical distribution of eolian sediment flux depends on local sediment supply. The MWACS were arrayed in a pattern designed to test specific hypotheses regarding the spatial distribution of eolian sediment fluxes described in section 3.2. At each tower and for each measurement interval the masses of eolian sediment trapped by each MWAC were plotted as a function of height above the ground to quantify the vertical distribution of eolian sediment fluxes. The particle-size distributions of 16 (i.e., four sets of vertical profiles) of the MWAC samples were measured using a Mastersizer 2000 laser-diffraction particle-size analyzer to determine the vertical variation in the diameter of transported particles.

2.3. Measurements of Yardang Morphology and Estimate of Topographic Diffusivity

The inputs for the morphological analyses include a 1-m/pixel DEM derived from airborne lidar data obtained from OWSVRA staff and a 0.02 m/pixel DEM of a subset of the area shown in Figure 3c that we constructed from a TLS survey conducted in October 2013 (see section 2.4 for description of these surveys). Two yardangs within the 0.02 m/pixel DEM derived from the TLS survey were analyzed to test the hypothesis that yardangs at OWSVRA could be characterized as asymmetric Gaussian functions.

A symmetric Gaussian is suggested by the topographic form of the cross section perpendicular to the wind illustrated in Figure 5b. However, yardangs are asymmetric in the along-wind direction. The term asymmetric Gaussian as used here refers to a 2-D Gaussian that is stretched in the downwind direction:

$$z = z_{max} \exp\left(-\left(\frac{x}{x_w}\right)^2 - \left(\frac{y}{x_w}\right)^2\right) \quad \text{if} \quad x < 0$$
$$= z_{max} \exp\left(-\left(\frac{x}{x_l}\right)^2 - \left(\frac{y}{x_w}\right)^2\right) \quad \text{if} \quad x \geq 0 \tag{2}$$

where z is elevation above the base of the yardang, z_{max} is the height of the yardang crest, x is the distance downwind from the yardang crest along the yardang axis, y is the distance from the yardang axis along a direction perpendicular to the axis, and x_l and x_w are characteristic dimensions of the yardang in the directions parallel and perpendicular to the wind, respectively. We extracted 15 topographic profiles perpendicular to the axis of the yardangs, 2 profiles on the lee side along the axis of each yardang, and fit the profiles to the respective 2-D profiles represented by equation (2).

The widths and lengths of yardangs were also extracted from Google Earth imagery by visual inspection. Also, the 1 m/pixel DEM derived from airborne lidar data was used to extract the heights, widths, and lengths of approximately 50 yardangs in the areas shown in Figure 3c. We developed a semiautomated procedure that accepts, as input, the location of a seed pixel within the DEM close to the crest of each yardang and works with this position to search the surrounding area within the DEM for all pixels connected (via one of the four nearest neighbors) to the seed pixel that have a negative curvature (Laplacian) or a slope gradient value that exceed user-defined threshold values. Searching refers to a recursive algorithm that finds the domain, connected to the seed, within which user-specified criteria are met. The crests of yardangs are characterized by significant negative curvature but generally low slopes (approaching zero at the crest), while the side slopes are characterized by the opposite: steep slopes but generally low curvature. By combining these two criteria, it is possible to use a high-resolution DEM to objectively determine the dimensions of each yardang. Although the threshold values of curvature and slope must be chosen by the user to obtain optimal results, we found that the results were not sensitive to those values within reasonable limits. The results presented in this paper were obtained using a threshold curvature of zero and a threshold slope gradient of 0.4 (22°). Given the set of pixels that represents each yardang determined by the algorithm (i.e., all of the pixels connected to the seed pixel with a negative curvature or a slope gradient of at least 0.4), the algorithm computes the length and width of each yardang as the maximum difference in pixel locations in the along-wind direction (to compute length) and the cross-wind direction (for width). The height is computed as the difference between the highest elevation and the lowest elevation within the set of pixels representing the yardang. Ehsani and Friedrich (2008) developed and applied a broadly similar algorithm to the megayardangs of the Lut Desert.

The numerical model developed in the companion paper includes a component that represents erosion by water-driven processes, including freeze-thaw-driven creep, rain splash, and interrill and rill erosion. As section 1.2.3 describes, the absence of vegetation and the relatively fine-grained nature of the siltstone and mudstone that dominate the Borrego Formation and the lee sides of yardangs in OWSVRA suggest that rain splash detachment of particles and the subsequent transport of detached particles by interrill and rill erosion are important processes on the tops and lee sides of yardangs. Assuming that the flux of sediment associated with water-driven processes depends linearly on slope gradient, conservation of mass implies a diffusion equation for topography (Culling, 1960):

$$\frac{\partial z}{\partial t} = D_{topo} \nabla^2 z \tag{3}$$

where z is elevation (m), t is time (kyr), and D_{topo} is the topographic diffusivity (m^2/kyr). If an average millennial-scale erosion rate can be estimated, the value of D_{topo} can be inferred as the ratio of the erosion rate to the average curvature on the leeward side of yardangs where water-driven processes are important and may be dominant:

$$D_{topo} = \frac{\partial z / \partial t}{\nabla^2 z} \tag{4}$$

The literature supports the utility of the diffusion equation for quantifying hillslope evolution by freeze-thaw-driven creep and rain splash, provided that slope gradients are modest (Dunne et al., 2010; Furbish et al., 2009; McKean et al., 1993). The slope dependence of sediment flux in interrill and rill erosion can also be

shown to be approximately linear. The Revised Universal Soil Loss Equation (RUSLE) predicts soil loss from hillslopes over time scales of single events, for which interrill and rill erosion, coupled with soil detachment by rain splash, are often dominant processes (United States Department of Agriculture - Agricultural Research Service, 2014). RUSLE uses a complex expression for the slope steepness factor (Nearing, 1997). However, Pelletier (2012; his Figure 1) showed that the slope steepness factor in RUSLE is closely approximated by a power law function of slope gradient with an exponent only modestly larger than 1 (i.e., 5/4). For the purposes of this and the companion paper (Pelletier, 2018), I assume that the slope dependence of interrill and rill erosion can be approximated by a linear dependence on slope gradient. Transport-limited conditions (i.e., deposition occurs in concave portions of the landscape) can be inferred from the presence of fan-shaped deposits at the base of many rills where the slope becomes concave. A linear dependence of sediment flux one slope gradient coupled with transport-limited conditions implies a diffusion equation for topography. Note that the rate of sediment transport by interrill and rill erosion can also depend on slope position, a point to which we will return in section 4.

2.4. Measurement of Topographic Change Using Multitemporal TLS

We conducted multitemporal TLS surveys of a portion of the yardang field illustrated in Figure 3c in October of 2013, 2014, and 2015. The purpose of these surveys was to measure erosion rates over time scales of ~1 year and compare them to the long-term rates estimated in section 1.2.1. In addition, we aimed to determine whether erosion occurs preferentially on the windward side of yardangs or more uniformly across the whole of each yardang. Given the high erosion rates measured over geologic time scales (3–4 mm/yr), together with the accuracy of the scanner under ideal conditions (2 mm), we hypothesized that it was possible to constrain erosion rates by differencing surveys conducted 1–2 years apart, provided that short-term erosion rates are comparable to long-term erosion rates.

We used a Leica C10 scanner to acquire TLS data at 40 stations within the survey area during each of the three surveys. The Leica C10 has an inherent surface-model accuracy of 2 mm under ideal conditions (a vegetation-free surface and calm winds) (Hodge et al., 2009). Windy conditions can introduce positional errors into TLS data, and vegetation cover introduces uncertainty into the process of constructing a bare-earth DEM from a point cloud. Our surveys were conducted under ideal conditions because (1) the yardangs we studied have no vegetation cover and (2) we were careful to survey on days with calm winds using a maximum scanner-to-target distance of 40 m. The resulting mean target registration error for the surveys was 2 mm, that is, the inherent scanner accuracy. The maximum target registration error was 4 mm, indicating that the errors associated with the point clouds of some individual scans were larger than 2 mm. However, our analysis is focused on quantifying changes in the mean elevation of the entire point cloud. As such, the mean target registration error is the most appropriate measure of uncertainty. A minimum of three Leica targets was used to register each scan to create a unified point cloud. The targets were located over drilled rebar posts that provided precisely the same set of targets for all three surveys. Bare-earth DEMs of 0.02 m/pixel resolution were created from the set of ground returns for each study site using an inverse-distance weighting (IDW) method (Liu et al., 2009). The bare-earth DEMs were differenced while within the reference frame of the fixed targets, that is, the rebar points. The difference maps were then registered to Real-Time Kinematic Global Positioning System (RTK-GPS) measurements of the target locations.

3. Results

3.1. Structural Data

The strikes and dips of resistant strata (Figures *6*a and *6*b) quantify the geometries of portions of the doubly plunging anticlines illustrated in Figures *3*b and *3*c. Strata mapped in Figure *6*a dip away from the anticline crest in all directions, with dip angles in the range of 17° to 40° for strata dipping to the east on the eastern limb of the fold and in the range of 43° to 61° for strata dipping to the north on the northern limb of the fold. The structural relationships of a portion of a doubly plunging anticline shown in Figure *3*b follow a similar pattern (Figure *6*b) with strata dipping to the southeast at angles ranging from 17° to 43° on the southeastern limb of the anticline and generally higher dip angles on more south dipping strata. Figures *6*a and *6*b suggest that yardangs tend to be more elongated, that is, have higher aspect ratios, where they strike more parallel to the prevailing wind direction. The data illustrated in Figure *6*a form the basis of a quantitative test of the structural control on yardang morphology presented in section 3.3.2.

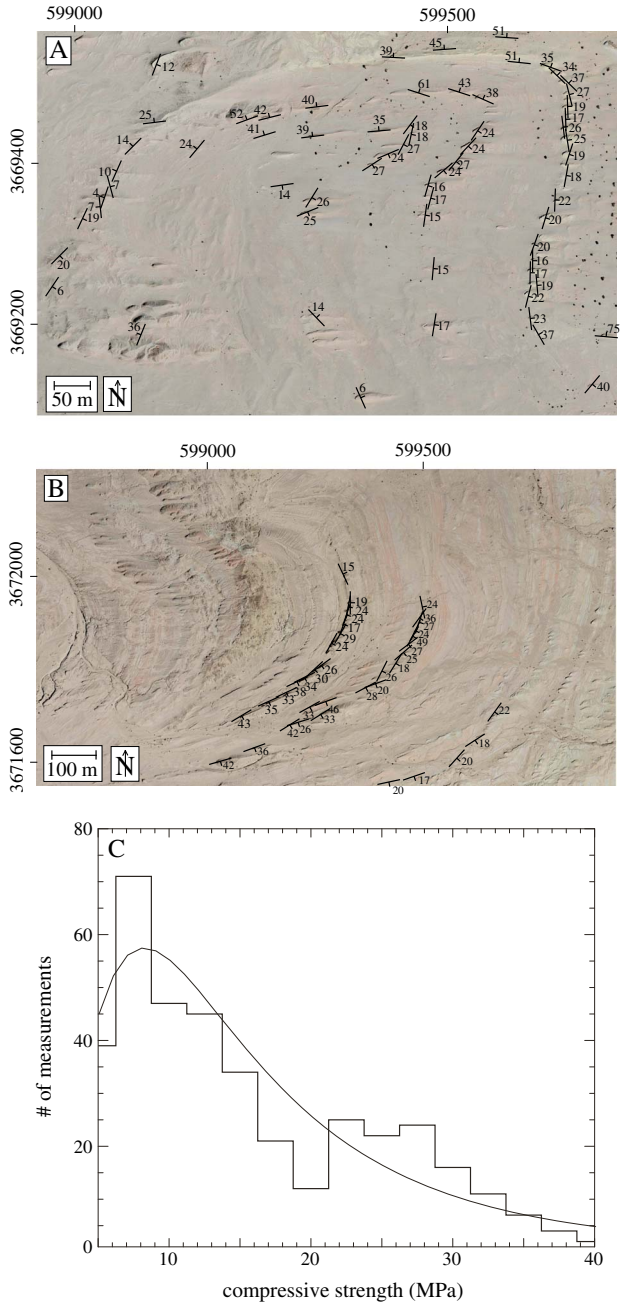

Figure 6. (a and b) Map of strike and dip angles of bedrock strata in the two yardang fields. (c) Frequency distribution of compressive strengths (measured via Schmidt hammer) of relatively resistant strata exposed on the windward sides of yardangs. Also shown is a lognormal distribution with a mean of 10 MPa and a coefficient of variation of 1.

The compressive strengths measured on sandstones range from approximately 5 to 50 MPa (Figure 6c; Table S1 in supporting information). The data are skewed toward lower values and approximately follow a lognormal distribution with a mean of 10 MPa and a coefficient of variation of 1 (Figure 6c).

3.2. Measurement and Analysis of Eolian Sediment Transport

3.2.1. Measurements of Sediment Flux

Figure 7a illustrates one of the eight MWAC towers used in this study. Figures 7b and 7c illustrate the locations of MWACS deployment. Both locations are a single pair of yardangs, relatively isolated from other topography. The locations differ in that one has sand sheets moving through the troughs during all of the collection intervals (Figure 7b), while the other was free of sediment storage both within the yardangs and for ~100 m upwind of the yardangs during all of the collection intervals (Figure 7c). The colors blue (Figure 7b) and red (Figure 7c) are used to associate the data (plotted in Figure 8) with the yardang pair around which they were collected.

The MWACS were deployed symmetrically around the northernmost yardang within each pair in the configuration shown in Figure 8. This arrangement features one MWAC tower located 3 m upwind from the yardang (location 1), four towers flanking the widest part of the yardang (two on each side; locations 2–5), two towers flanking the narrower part of the yardang approximately midway between the widest portion of the yardang and the tail (locations 6 and 7), and a final location at the tail (location 8). This arrangement is symmetrical except for the presence of another yardang to the south and the absence of a neighboring yardang to the north.

We hypothesized that eolian sediment fluxes would be highest close to the yardang at its widest point (locations 3 and 4) because these locations accommodate wind and sediment deflected around the windward face. Similarly, we hypothesized that locations 2 and 5 would have a relatively high eolian sediment flux, but marginally lower than locations 3 and 4 because they are farther from the yardang. We expected the eolian sediment flux at locations 6 and 7 to be somewhat higher than location 1, but smaller than locations 2–5, because they are in the trough but located toward the tail where the trough is less topographically confined. Finally, we hypothesized that location 8, situated in the wake of the yardang ridge, would have the lowest flux. We also hypothesized that eolian sediment fluxes would be higher at locations on the south side of the yardang (i.e., between the two yardangs) compared to the analogous locations across the yardang axis on the north side, as a result of the additional deflection of wind and sediment into the trough between two yardangs compared to the flank of just a single yardang.

Figure 8 plots the mass of sediment trapped in the MWAC located 0.21 m above the ground at each location for the five time intervals between May and June of 2015. We did not observe any significant difference in the patterns of sediment flux between the two areas, indicating that the patterns we observed were robust with respect to whether the environment is locally supply limited (Figure 7c, red) or not (Figure 7b, blue). Data plotted in black are the average for the five time intervals. The data have been normalized to the mass of sediment trapped at location 1 positioned 3 m upwind from the yardang. As such, the bar chart next to location 1 shows a value of 1 for all five time intervals. As expected, the mass of sediment moving past locations 2–5 is larger than all other locations. Among locations 2–5, the average mass of trapped sediment was higher closer to the yardang (locations 3 and 4) compared to

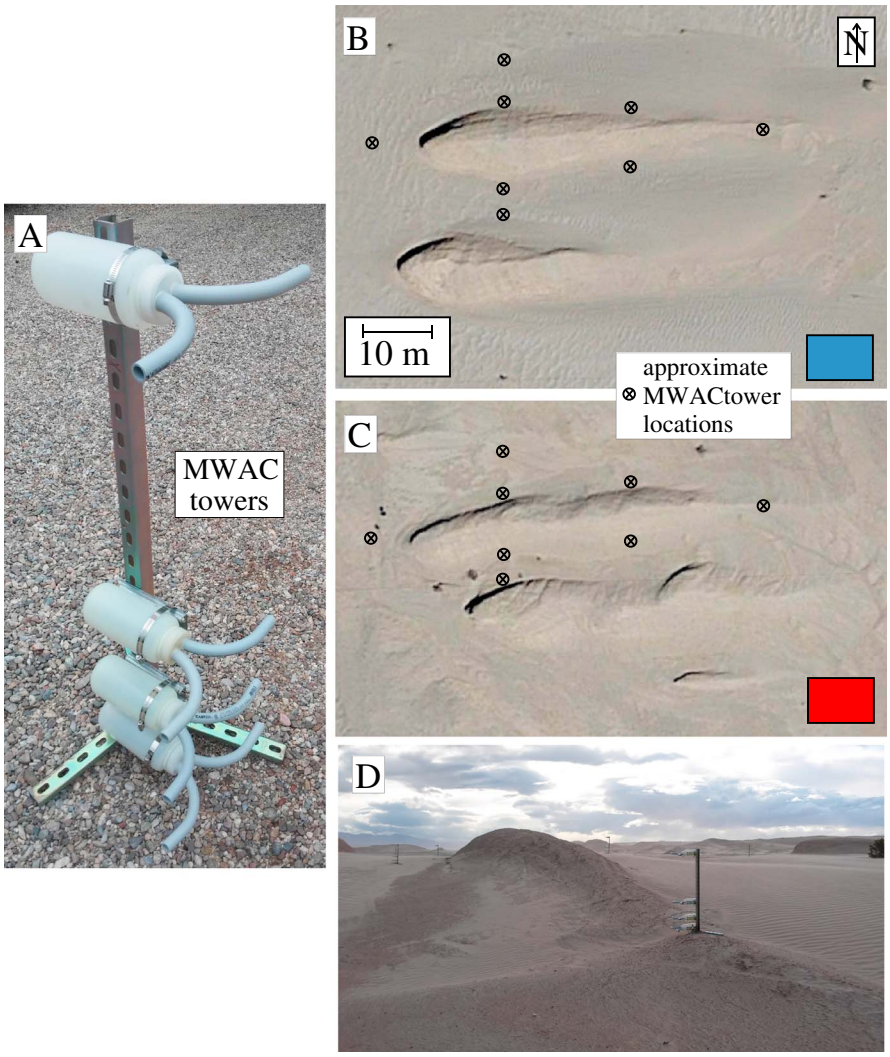

Figure 7. Photographs illustrating the MWACS and the locations of their deployment around yardang pairs. (a) Close-up of a MWAC tower (ground surface pictured is not in the field area). (b) Northern location (where sand sheets occur in trough). (c) Southern location (no sand sheets). (d) View looking upwind with four MWACS visible around the northern yardang of the area illustrated in (b).

locations farther from the yardang (locations 2 and 5) at the widest part of the yardang. Also, there was higher eolian sediment flux on the south side of the yardang (locations 2 and 3) compared to locations on the north side (locations 4 and 5), as hypothesized. Locations 6 and 7 had higher eolian sediment fluxes than location 1 and were nearly identical to each other, consistent with the fact that the effect of the yardang to the south in focusing sediment into the trough has a diminishing effect toward the tail of the yardang because the trough is less topographically confined toward the tail. Location 8 had, on average, less than half of the eolian sediment flux of location 1.

The vertical profile of eolian sediment flux, q_s, follows a power law function of height above the ground, z, for distances from 0.09 and 1.02 m, that is,

$$q_s(z) \propto z^{-b} \tag{5}$$

where b has a mean value, determined by least squares regression of each vertical profile, equal to 2.5 ± 0.1 (Figures 9a and 9b; 0.1 represents the standard deviation of the regression coefficients for each data profile) (Table S2 in supporting information). In Figure 9, the same data are plotted three ways. In Figure 9a, all of the raw data are plotted. The measured masses range from approximately 0.2 g to 1 kg. Lines connecting the circles link the data collected at the same tower for the same time interval of measurement. If all MWACS recorded a finite amount of sediment, all of the profiles in Figure 9a would have four data points.

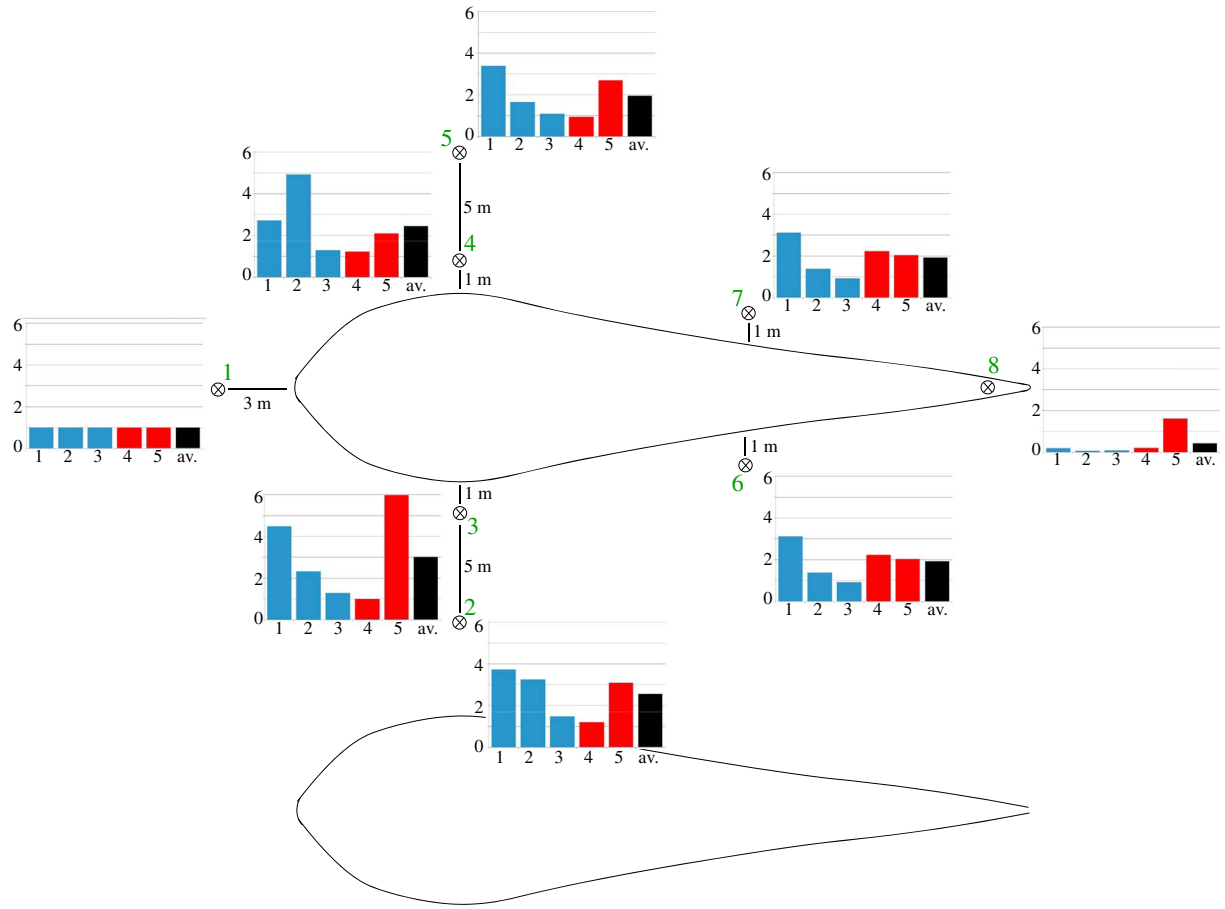

Figure 8. Diagram illustrating the relative eolian sediment flux 20 cm above the ground as a function of time and position around nearby yardangs. Each graph shows the eolian sediment flux (relative to the windward position) at each of five measurement intervals, plus the average of the five time intervals. Blue bars correspond to the yardangs illustrated in Figure 7a, while red bars correspond to the yardangs illustrated in Figure 7b.

However, there are three plots for which the amount of sediment was below the minimum amount that could be measured (0.2 g) at 1.02 m above the ground. At the other end of the spectrum, bottles with more than 1 kg of sediment likely represent minimum values. This is because bottles that are more than half full can impede the flow of air into the bottle. Figure 9b plots the same data as Figure 9a except that the data have been normalized so that the mass of sediment trapped in the MWAC is set to be 10 g. We normalized the data in this way because our goal was to constrain the shape of the vertical profile of eolian sediment flux (absolute values of flux are less relevant as we did not simultaneously measure wind conditions). Figure 9b highlights the similarity in the shape of the sediment flux profile despite large variations in wind conditions among the five time intervals of measurement (Figure 9a). Figure 9c plots the same data on log linear scales in order to demonstrate that the data are not well represented by an exponential function. The mean R^2 value for the power law relationship (equation (5)) is 0.85, while the mean value for the exponential relationship is 0.35. Note that the fact that some samples may be minimum values cannot be the reason for the poor fit to an exponential profile, since an increase in the mass of trapped sand at the lowest distance from the ground would only make the deviation of the data from an exponential trend (Figure 9c) worse. It should be emphasized that the power law relationship of equation (5) applies only over the range of distances above the ground we measured.

3.2.2. Measurements of the Aerodynamic Roughness Length

In order to estimate the appropriate values of the aerodynamic roughness length for input to the numerical model presented in the companion paper (Pelletier, 2018), we measured wind profiles on a rippled low-relief sand sheet approximately 5 km downwind from the yardang field during three wind events during the spring of 2015 and fit them to the fully rough form of the law of the wall:

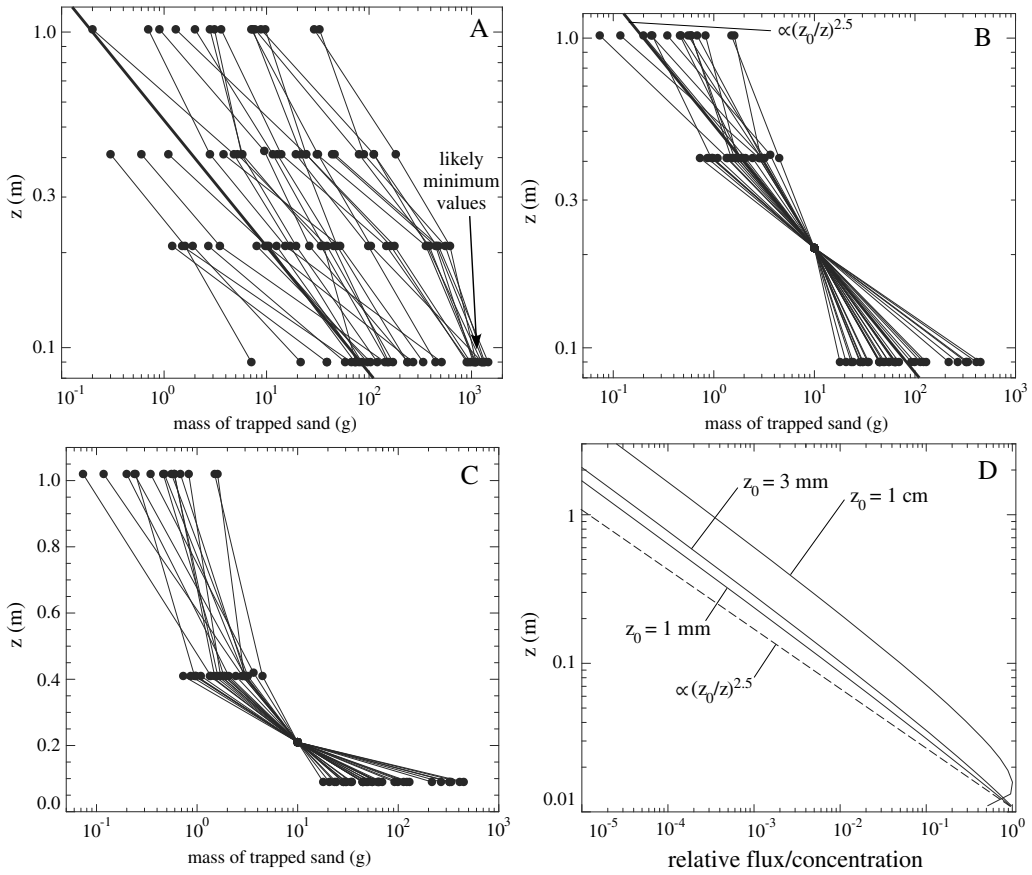

Figure 9. Plots of measured eolian sediment fluxes and modeled fluxes and concentration profiles as a function of height above the ground. (a) Raw measured data for eolian sediment flux. (b) Data normalized so that the trapped sand 20 cm above the ground is equal to 10 g for all the plots. This set of plots isolates the shape of the vertical profile by minimizing differences in the absolute value of flux among profiles. The thick line corresponds to a power law relationship with exponent of −2.5. Note the logarithmic scales on both axes. (c) Same data as (b), except plotted using log linear scaling to demonstrate the poor fit of the data to an exponential function. (d) Plots of relative concentration predicted by the advection-diffusion-settling model with Rouse number of 2.5 (dashed line) and relative flux profiles for three values of the aerodynamic roughness length, z_0. All plots in (d) are set to have a maximum value of 1 at $z = 0.01$ m or their maximum value above that height.

$$u(z) = \frac{u_*}{\kappa} \ln\left(\frac{z}{z_0}\right) \tag{6}$$

where $u(z)$ is the wind velocity at a height z above the bed, u_* is the shear velocity, κ is the von Kármán constant (0.41), and z_0 is the aerodynamic roughness length. The location for these measurements (33°11, 015′N; 115°51, 921′W) was carefully chosen to ensure an equilibrium between the local surface roughness and boundary layer development. The location is a sand sheet with ~10 cm of relief over an area approximately 30 m long (length parallel to prevailing winds) by 20 m wide with a nearly uniform ripple geometry. Wind speeds were measured at 12-s intervals and at four heights above the ground (0.185 m, 0.52 m, 1.22 m, and 2.80 m) using four Inspeed Vortex rotating cup anemometers. The average wind speed during the monitoring period was approximately 6.5 m/s at 1.2 m above the surface, with gusts commonly exceeding 12 m/s. Shear velocities and roughness lengths were calculated via least squares fitting of the wind velocities to the natural logarithm of the height where the wind speed was measured. Shear velocities were calculated as the inverse of the slope of wind speed u versus ln z, multiplied by the von Kármán constant. The value of z_0 was calculated as the exponential of the intercept. Only wind profiles that fit the law of the wall with R^2 greater than 0.95 were retained for analysis.

Measured values of z_0 vary from approximately 0.1–3 mm, with higher values characteristic of faster winds and more vigorous sediment transport. Figure 10 demonstrates that the data are reasonably well fit by several empirical models that seek to quantify saltation-induced roughness, including Charnock (1955), Raupach (1991), and Sherman (1992). For example, the Sherman relationship, that is,

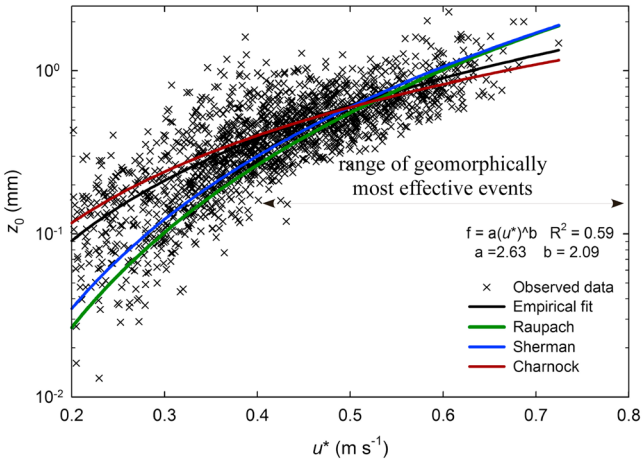

Figure 10. Measured values of z_0 as a function of shear velocity. The red line represents the best empirical fit for the observed data. The green, blue, and black lines represent model predictions based on the Raupach (1991), Sherman (1992), and Charnock (1955) relationships.

$$z_0 = (\alpha/g)(u_* - u_{*t})^2 \quad (7)$$

where g is the acceleration due to gravity, can be reasonably well fit to our data ($R^2 = 0.56$) with a value of α equal to 0.063 for $u_{*t} = 0.2$ m/s. This value of α is somewhat smaller than the value of 0.132 that Sherman and Farrell (2008) obtained from their analysis of field data reported in the literature. However, some variation in the value of α between sites is expected due to the fact that saltation-induced roughness likely depends on grain size and the geometry of bedforms that evolve during sediment transport.

Values of z_0 are highly dynamic since z_0 is a nonlinear function of shear velocity and shear velocity varies over time scales as small as minutes or even seconds. The numerical model of the companion paper (Pelletier, 2018) requires a value of z_0 as input, but the model cannot resolve each and every variation in wind speed in order to model yardang formation over time scales of millennia. As such, it is necessary to estimate the z_0 value or range of values associated with the geomorphically most effective wind speed (or range of speeds) and use that value or range of values as representative of the wind speed(s) that contribute most to the long-term abrasive erosion of the landscape. The geomorphically most effective wind speed is the speed that contributes most to the long-term average erosion, taking into account the frequency of events (which decreases with increasing wind speed) and the relative effectiveness of each speed (which increases with speed). To estimate the value of z_0 associated with the geomorphically most effective wind events, we estimated 6 years of shear velocities using 15-min average wind speeds measured 10 m above the ground at CWOP DW1021 from 2009 to 2015. The shear velocity is a function of z_0 (equation (6)), but z_0 is also a function of shear velocity (equation (7)). As such, we used equations (6) and (7) iteratively by first assuming a default value z_0 value of 0.01 mm to estimate u_* using equation (6) then updating the value of z_0 and u_* iteratively until convergence was achieved.

Eolian abrasion rate scales approximately with fifth power of shear velocity (Anderson, 1986):

$$E \propto u_*^5 \quad (8)$$

Equation (8) relies upon several assumptions, including that sand transport scales with the cube of shear velocity and abrasion rate depends linearly on the particle kinetic energy, neither of which may apply precisely. For example, it has been argued that sand transport rates scale with the square of shear velocity (Martin & Kok, 2017). With that caveat noted, Figure 4c plots the relative frequency of shear velocities and the geomorphic effectiveness (defined here as the product of the frequency of shear velocities and the fifth power of the shear velocity according to equation (8)) for each shear velocity assuming equation (8) applies. The geomorphic effectiveness has a broad maximum over a range of shear velocities from 0.4 to 0.8 m/s. This range of shear velocities has an optimum combination of frequency and geomorphic effectiveness per event or per unit time that, collectively, makes this range of shear velocities the most geomorphically effective. Values of z_0 values are time dependent since they depend on transport conditions. The z_0 value most relevant to long-term yardang evolution is the z_0 of the geomorphically most effective wind storm. Figure 10 demonstrates that z_0 values corresponding to shear velocities from 0.4 to 0.8 m/s are generally in the range of 0.3–3 mm. As such, we propose that z_0 values in the range of 0.3–3 mm are representative of the geomorphically most effective wind events in the study site.

3.2.3. Measurements of the Grain Size Profile

Figure 11a plots the particle size distributions of four sets of vertical profiles of eolian sediment collected by the MWACS (Table S3 in supporting information). Samples closer to the ground are shown with thicker curves. In all four sets of profiles there is a general tendency for the sediment to be finer higher above the ground. Figure 11b plots the median grain diameter (x axis) as a function of height above the ground (y axis). The filled circles are all the data (one data point each for 16 samples), and the larger unfilled circles correspond to the average of the median grain size for each height (0.09, 0.21, 0.42, and 1.02 m above the ground). The median grain diameter at 0.1 to 1 m above the ground is in the range of approximately 80–120 μm. Grains of this size are expected to be in modified saltation (i.e., transported via semirandom trajectories

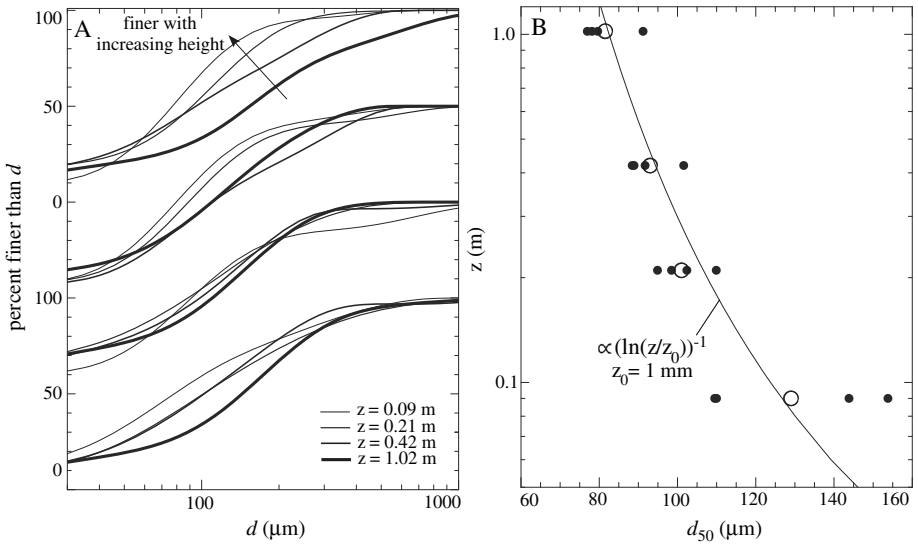

Figure 11. Grain size data. (a) Plots of the cumulative particle size distribution for four of the sampled profiles. The line with arrow indicates the general trend of the data toward finer sediment for increasing distances above the bed. (b) Plots of median grain diameter, d_{50}, versus height above the bed, z, for the same data plotted in (a). The small filled circles show all of the data; the larger open circles represent the average for each height. The data are consistent with an inverse logarithmic profile.

influenced by both inertia and terminal velocity) or short-term suspension when u_* exceeds 0.4 m/s for the smaller end of median grain sizes and when u_* exceeds 0.7 m/s for the larger end of median grain sizes (Figure 8 ofÚjvári et al., 2016). Both of these shear velocities are close to or within the range of geomorphically most effective shear velocities for the study site. The median grain size follows a relationship

$$d_{50} = \frac{d_{50}(z_0)}{\ln\left(\frac{z}{z_0}\right)} \tag{9}$$

as plotted in Figure 11b.

3.2.4. Comparison of the Sediment Transport Profile With Theoretical Models

A power law vertical distribution of sediment flux is consistent with theoretical models of eolian sediment transport near the saltation-suspension transition. To show this, first we consider a model for the vertical profile of eolian sediment concentration. The traditional model for the concentration, $c(x,z)$, of sediment transported by wind or water is the advection-diffusion equation with gravitational settling:

$$u(z)\frac{\partial c}{\partial x} = \frac{\partial}{\partial z}\left(D(z)\frac{\partial c}{\partial z}\right) + w_s\frac{\partial c}{\partial z} \tag{10}$$

where $u(z)$ is the time-averaged wind speed at height z, $D(z)$ is the vertical diffusivity of the sediment in transport, and w_s is the average settling velocity of the grains. In the eolian case this model was first explored by Sundborg (1955) and later by Anderson and Hallet (1986). Assuming a steady state balance and no horizontal variation in concentration, equation (10) becomes

$$\frac{\partial}{\partial z}\left(D(z)\frac{\partial c}{\partial z}\right) = -w_s\frac{\partial c}{\partial z} \tag{11}$$

The sediment diffusivity can be approximated by $\kappa u_* z$, which yields the solution (Anderson & Hallet, 1986; Sundborg, 1955)

$$c(z) = c(z_0)\left(\frac{z_0}{z}\right)^{R_\#} \tag{12}$$

where $R_\#$ is the Rouse number defined as $w_s/\kappa u_*$. A Rouse number of 2.5 is associated with the transition from bed load to suspended load. As such, the vertical distribution of eolian sediment flux we measured (equation (5) with b = 2.5) is identical to the vertical distribution of concentration predicted by the advection-diffusion-settling model for sediment transported near the saltation-suspension transition. A

factor of β is often introduced into the definition of $D(z)$ to quantify potential differences between the eddy (momentum) diffusivity and the sediment (mass) diffusivity (see Farrell, 2012, for a discussion). No such factor is included here because equation (12) reproduces the trends in our data.

The flux profile and the concentration profile are not the same, but they scale similarly with the height above the ground for the range of heights we measured and for the values of z_0 applicable to the study site. To show this, we first note that the volumetric sediment flux is equal to the product of sediment concentration and grain velocity:

$$q_s(z) = c(z)u(z) \tag{13}$$

If the grain velocity is assumed to be similar to the wind velocity (i.e., not precisely equal to the wind velocity but exhibiting a similar vertical profile), $u(z)$ can be estimated using equation (6). Figure *9*d plots both the flux profile (solid curve) predicted by equations (10)–(12) together with the concentration profile (dashed curve) predicted by equation (10) for a range of values of z_0. For z_0 values of 1 mm or less, the velocity varies little from distances of 0.1 to 1 m above the ground compared to the concentration (i.e., ln(1/0.001) and ln(0.1/0.001) differ by only 50% while the concentration differs by a factor of 300). Hence, the concentration profile and flux profile scale similarly with height for all but the lowest heights above the ground. As the value of z_0 increases, the difference between the flux and concentration profiles becomes more substantial. For a z_0 value of 1 cm (which would be considered on the high end of possible values for the study site), the relative flux and concentration profiles differ substantially at heights less than 5 cm, with the flux profile developing a peak at approximately 2–3 cm above the ground. Given that z_0 values in the study area are ~1 mm, we conclude that the flux and concentration profiles should have almost the same dependence on height for the heights above the ground we measured, that is, between 0.1 and 1 m. This similarity enables us to conclude that evidence for a power law dependence of flux on height with an exponent of -2.5 is evidence for a concentration profile with the same dependence on height over the range of heights we measured.

The results presented in this section would not change substantially if grain velocities differed from wind velocities by a constant fraction since the grain velocity would still follow the logarithmic dependence on height given by equation (6). If, however, the relative speed of wind and sediment varies substantially with height, the relative concentration and flux profiles could differ more than shown in Figure *9*d. We propose that any such difference is likely to be relatively small, however. For example, Rasmussen and Sørensen (2008) measured the ratio of particle speed to wind speed to be ≈0.5 very close to the surface (5 mm), with values increasing to nearly 1 (i.e., 0.8–0.9) at heights of only 8 cm above the bed.

3.3. Measurements of Yardang Morphology and Estimate of Topographic Diffusivity

3.3.1. Yardangs as Asymmetric Gaussians

Figure 12 illustrates the results of our attempt to fit the topographic profiles of yardangs to an asymmetric Gaussian function (equation (2)). Figure 12a is a shaded-relief image of a portion of the 0.02 m/pixel DEM derived from the 2013 TLS survey. Overlain on this image are the locations of the seventeen profiles extracted and fit to 1-D profiles of equation (2). Figure 12b is a shaded-relief image (with contours overlain) of equation (2) with aspect ratios of 2, 4, and 8. Figure 12c plots the 15 profiles perpendicular to the wind, normalized so that with z_{max} = 1 m and x_w = 1 m, along with the associated profile of equation (2) for comparison. The plots in Figures 12c and 12d demonstrate that equation (2) represents the shapes of these yardangs well. Figure 12c, in particular, shows that the profiles have a universal functional form despite large differences in the scale of the profiles; that is, profiles close to the tail are narrower and shorter than profiles close to the yardang crest, yet all are well represented by a Gaussian function. We also performed the same analysis on two other pairs of yardangs and obtained results that are visually similar to those of Figure 12.

Figure 13a presents the results of the semiautomated mapping algorithm on the yardang field illustrated in Figures *3*c. The domains mapped by the algorithm as yardangs are shown using a darker shade of gray. Since the algorithm requires an initial seed location from which to search the surrounding area in the DEM, Figure 13a shows only the yardangs that we selected for analysis, that is, yardangs where structure data were collected and that otherwise had a distinctive yardang-like shape.

3.3.2. Controls on Yardang Extents and Aspect Ratios

Figure 13b compares the aspect ratios computed by the semiautomated algorithm to those computed visually (Table S4 in supporting information). The two methods agree to within 30% in more than half of

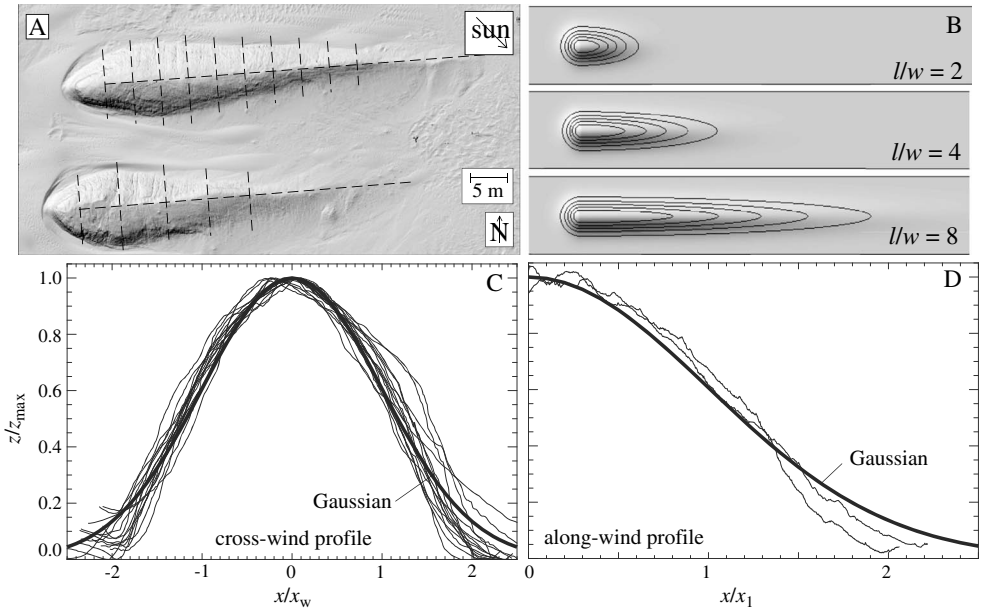

Figure 12. Asymmetric Gaussian shape of yardangs at Ocotillo Wells. (a) Shaded-relief image of two yardangs chosen for analysis. (b) Shaded-relief image (with contours overlain) of yardangs modeled as an asymmetric Gaussians (equation (2)). (c) Plots of normalized topographic profiles perpendicular to the wind (thick curve is the asymmetric Gaussian). (d) Plots of normalized topographic profiles parallel to the wind.

cases. The data show the most significant deviation for yardangs of low aspect ratio. For these cases, the visual method tends to estimate a higher aspect ratio relative to the semiautomated method. This could be because the semiautomated method is less adept than the eye at mapping the full extent of yardang tails (where slopes

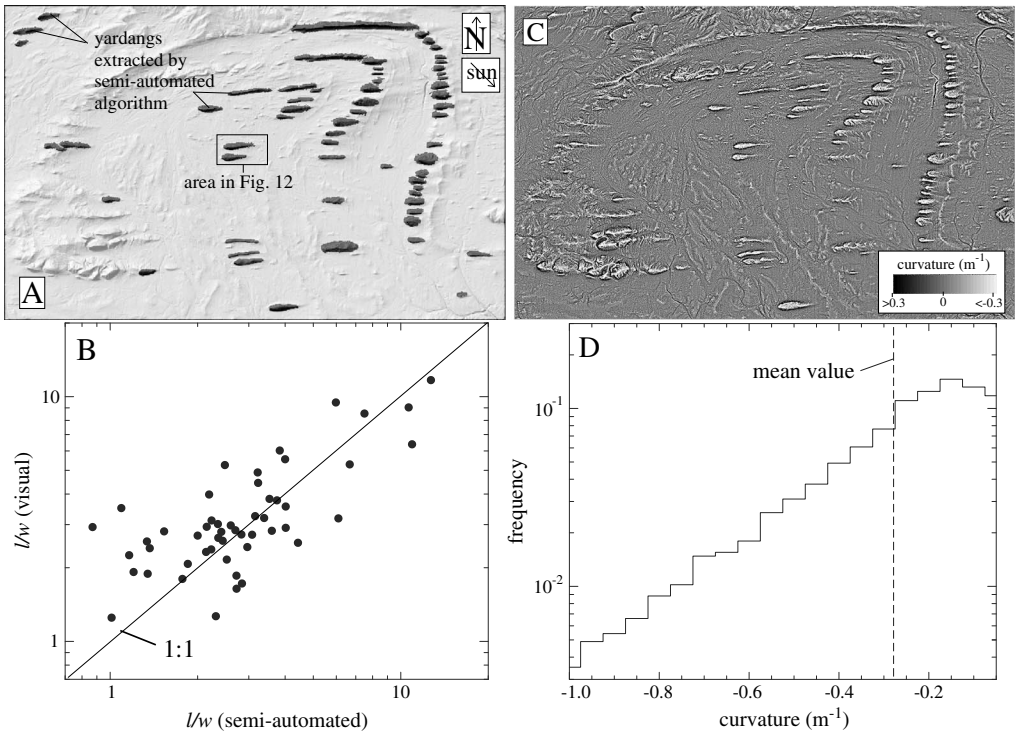

Figure 13. Example results of the semiautomated mapping algorithm and the curvature data used to estimate topographic diffusivity. (a) Shaded-relief image of the southern yardang field at Ocotillo Wells, overlain with a partially transparent mask of the extracted yardangs. (b) Plot of the aspect ratio (i.e., length-to-width ratio) of the yardangs extracted by the semiautomated algorithm versus those extracted by eye. (c) Map of the topographic curvature (Laplacian) of the yardang field illustrated in (a). (d) Plot of the histogram of negative curvature values from just the yardang areas (shown in black) from (a). The mean curvature value is $-0.27\ m^{-1}$.

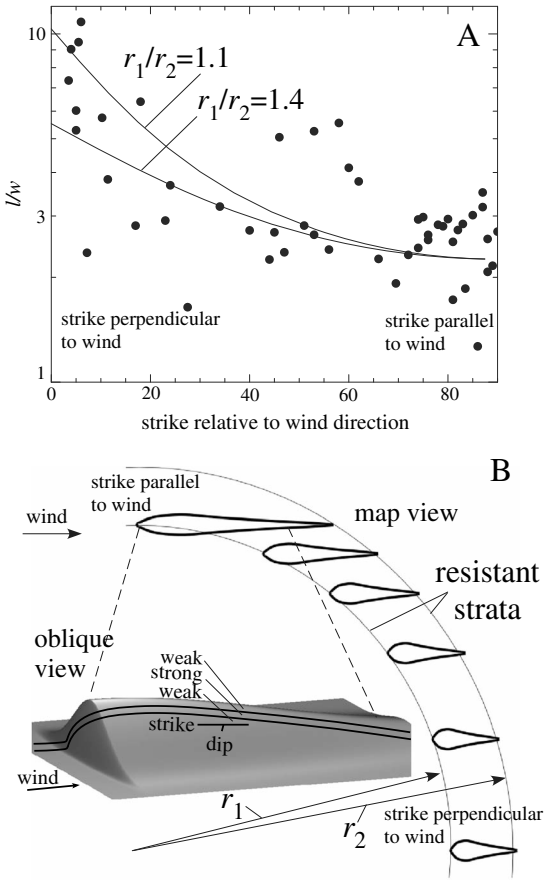

Figure 14. Documentation of the relationship between yardang aspect ratio and the strike direction with respect to the wind. (a) Plot of aspect ratio, *l*/*w*, versus the strike direction relative to the wind. Also plotted are the predictions of equations (14) and (15) for two different values of the ratio of radii characterizing the map view geometry of the beds sufficiently resistant to trigger yardang development. (b) Schematic diagram illustrating how the strike direction relative to the wind may control the along-wind distance (and hence yardang aspect ratio) between resistant beds that trigger yardang formation.

decrease asymptotically to zero). The fact that the two methods yield similar results provides a basis for using the semiautomated algorithm in future studies of large yardang fields for which visually measuring every yardang would be impractical and 30% accuracy is acceptable. In this study, we used the length and width of yardangs measured visually together with the height of yardangs measured by the semiautomated method in all subsequent analyses.

An inverse relationship exists among yardang aspect ratios and the local strikes of bedrock strata relative to the wind (Figure 14a). Figure 14b presents a conceptual model for how the strike relative to the prevailing wind direction may control yardang aspect ratios. This model assumes that yardang formation in OWSVRA is triggered by the exhumation of resistant beds within portions of the stratigraphy (i.e., Borrego Formation) that contain interbedded sandstones and siltstones/mudstones. This assumption is consistent with the observation that a sandstone bed with a compressive strength of at least 5 MPa is exposed on the windward side of every yardang in the study site. In this conceptual model, yardang lengths are constrained by the along-wind distance between beds that are sufficiently resistant to trigger yardang development. Where the resistant beds strike perpendicular to the wind, the distance between such beds is relatively small. Conversely, where beds resistant enough to trigger yardang formation strike parallel to the wind direction, the distance is relatively large (Figure 14b).

The relationship between yardang length and the strike direction relative to the wind can be determined quantitatively for cases in which the outcrops of the sufficiently resistant beds are circular in map view. If the beds that trigger yardang development outcrop along circular arcs with radii r_1 and r_2, the distance between these beds along the wind direction, $x_2 - x_1$, (i.e., the yardang length) is given by

$$x_2 - x_1 = \sqrt{r_2^2 - r_1^2 + x_1^2} - x_1 \tag{14}$$

and the strike relative to the wind, δ, is given by

$$\delta = \text{atan}\left(\frac{x_1}{\sqrt{r_1^2 - x_1^2}}\right) \tag{15}$$

A plot of the distance along the wind direction between beds sufficiently resistant to trigger yardang development (a proxy for yardang length) versus the strike direction relative to the wind can be made by evaluating equations (14) and (15) for a range of values of x_1 from 0 to r_1. To associate $x_2 - x_1$ with an aspect ratio, we divided $x_2 - x_1$ by a constant width, the value of which was chosen to yield an aspect ratio of 2.5 at a strike direction of 90° (2.5 plots within the center of the cloud of data associated with large relative strike angles in Figure 14a). Figure 14a plots the results of equations (14) and (15) for r_1/r_2 = 1.1 and 1.4. Both curves exhibit a nonlinear increase in aspect ratio similar to the data as the strike direction relative to the wind direction approaches zero.

The increase in aspect ratio in yardangs with resistant beds that strike nearly parallel with the wind may also be due partly to the geometry of the resistant bed within those yardangs (oblique view image in Figure 14b). When wind and wind-blown sediments approach a resistant bed that strikes nearly parallel to the wind, the heterogeneity of the substrate enhances the feedbacks among topography and the spatial variations in wind speeds, eolian sediment fluxes, and erosion rates. Wind-blown sediments are diverted around the resistant

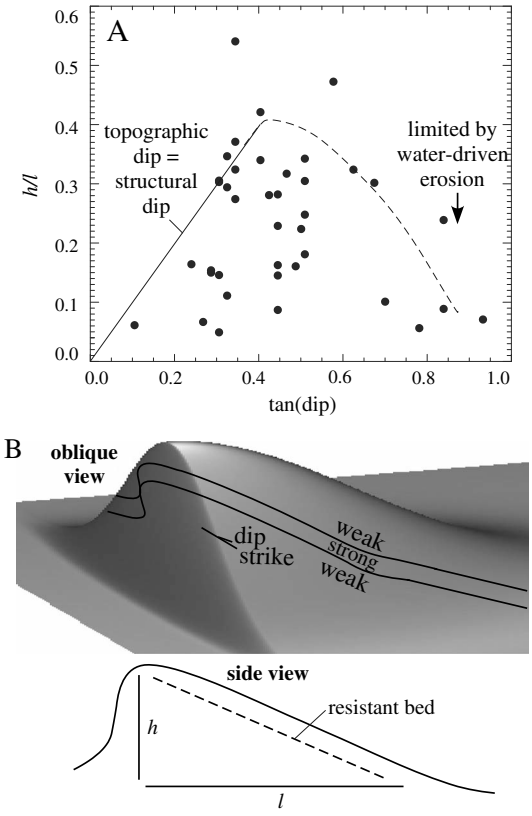

Figure 15. Documentation of the relationship between yardang height-to-length ratio and the tangent of the structural dip. (a) Plot of the height-to-length ratio as a function of the tangent of the dip. Yardangs with tan(dip) of less than approximately 0.4 have *h/l* values that are similar to (but somewhat less than) tan(dip), while yardangs with steeper dips (which tend to be longer) have *h/l* values that are much lower because their heights are limited by water-driven erosional processes. (b) Schematic diagram of how the height-to-length ratio can be controlled by the tangent of the dip.

bed where they incise readily into the weaker beds flanking the resistant bed. As such, erosive power is maximized where the substrate is weakest and minimized where it is strongest. The result is a yardang with a large aspect ratio that may parallel the bedrock structure for a long distance.

In the field we noted that the topographic dips of yardangs tend to follow the structural dips, that is, that yardangs with steeply dipping resistant layers tend to have steep slopes subparallel to the structural dip. Figure 15b shows this schematically. If erosion occurs rapidly in the weak strata overlying the resistant bed, the surface will encounter the resistant bed and erosion will slow, thereby leading to a similar dip between resistant bed and the top and lee sides of the yardang. The ratio *h/l* tends to correlate positively with tan(dip) for tan(dip) values less than approximately 0.4 (Figure 15a). In these yardangs, yardang height is partially controlled by structure, with more steeply resistant beds tending to form more steeply dipping slopes down the lee sides of yardangs. Above tan(dip) values of approximately 0.4, *h/l* values are much smaller. These yardangs tend to be the longest yardangs in the study area; that is, steeply dipping yardangs tend to be ones with strata that strike nearly parallel to the wind. In these cases, mass wasting and/or water-driven erosion may be a limiting factor on yardang height. For example, a yardang 5-m wide, 50-m long and with tan(dip) of close to 1 would have to be 50-m tall in order for the linear relationship between *h/l* and tan(dip) to hold across the full range of yardang shapes and sizes. This would result in side slopes in excess of 85°. Mass wasting and water-driven erosion preclude the development of yardangs that are this tall or steep.

Figure 16a plots yardang heights versus widths on logarithmic scales. The data follow a square root relationship, indicating that wider yardangs have side slopes that are generally less steep than narrower yardangs. Structural control is one potential explanation for this lack of self-similarity. If taller yardangs are associated with resistant beds that are thicker and/or more resistant (illustrated in Figure 16b with a darker gray) than those of shorter yardangs, taller yardangs will likely have flatter tops as rapid erosion of weaker beds exposes the relatively wide and more resistant bed associated with taller yardangs (Figure 16b). Such a flattening is implied by the lack of self-similarity between yardang height and width and is consistent with observations in the field (i.e., it is much easier to walk along the crestline of taller yardangs, since the crests are flatter; shorter yardangs more commonly have knife-edge crestlines). Another factor that may contribute to the sublinear scaling of yardang height with width is the fact that water-driven erosional processes tend to be more effective on longer slopes (e.g., McCool et al., 1989). This would increase the effective topographic diffusivity of wider yardangs relative to shorter yardangs, causing their height to increase more slowly with increasing width than our diffusion model with uniform diffusivity would predict.

Figure 17 demonstrates, using three rows of yardangs selected from the study area, that mean yardang spacing is nearly proportional to width. These rows of yardangs were chosen to represent a range of yardang sizes, from a low value of 5 m to a high value of approximately 20 m. The yardangs shown in Figure 17a are less ideally shaped than other yardangs we considered, but they were included in order to provide a large-yardang end-member in the analysis. The profiles shown in Figure 17c were subdivided into three profiles in order to treat two areas of small yardangs separately, further widening the range of yardang sizes considered. The data exhibit a nearly linear relationship between mean yardang spacing and width (Figure 17e) with a coefficient of proportionality of 1.5 determined from a linear regression with least squares error.

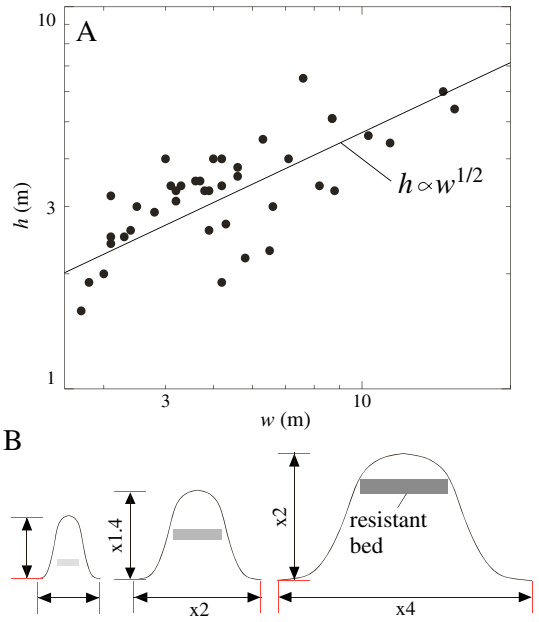

Figure 16. Documentation of the lack of self-similarity in the relationship between yardang heights and widths. (a) Yardang height increases with the square root of width, indicating that wider yardangs have lower slopes, on average. (b) Schematic diagram of how thicker and/or more resistant beds associated with taller beds may have lower slopes.

3.3.3. Estimate of the Topographic Diffusivity

Figures 13c and 13d illustrate the calculations made to estimate the topographic diffusivity D_{topo}. The starting point for this calculation is the fact that long-term erosion rates are approximately 3–4 mm/yr (section 1.2.1). Next, we mapped the topographic curvature (Laplacian) as shown in the gray scale map in Figure 13c. Then, we extracted values of the curvature from just the areas of the yardangs (as identified by the semiautomated algorithm shown in Figure 13a). Figure 13d plots the frequency distribution of curvature values from yardangs. Curvature values vary from approximately -0.1 to -1 m^{-1}, with values closer to -0.1 more common. The mean value is -0.27 m^{-1}. Using 3–4 mm/yr as an estimate of the erosion rate and -0.27 m^{-1} for the curvature yields an estimate from equation (4) of approximately 1 m^2/kyr for D_{topo}. This estimate assumes that the modern curvature is representative of the curvature over geologic time, thus allowing the long-term relationship between erosion rate and curvature to be defined by an effective D_{topo} value. This value is consistent with D_{topo} reported in the literature from semiarid environments (Hanks, 2000). Hanks (2000) compiled data on values of κ inferred from the degradation of landforms of known age (e.g., pluvial shoreline scarps). The values of κ reported by Hanks (2000) increase systematically in more humid climates: that is, D_{topo} = 0.1–0.7 m^2/kyr in the hyperarid and arid portions of Israel and D_{topo} = 0.5–2.0 m^2/kyr in the semiarid portions of the western U.S.

3.4. Measurements of Topographic Change Using Multitemporal TLS

Figure 18 displays the design and results of the TLS survey of 2013. The surveys of 2014 and 2015 were essentially identical, as the targets were in the same locations (within 1 mm, carefully positioned over drilled rebar) and the scan stations also had the same locations within hand-held GPS accuracy as the 2013 survey. Figure 18a is a map of the point density of the survey (note logarithmic scale). For the purposes of detecting topographic changes, we considered areas with more than 10^3 returns m^{-2} to be sufficiently dense for accurate change detection. Figures 18b and 18c illustrate the shaded-relief image of the DEM constructed from the point cloud using the IDW technique.

Figure 19a illustrates the topographic change between 2013 and 2015. Areas that underwent negative topographic changes are eroding, while areas that underwent positive topographic changes are aggrading. Figure 19b illustrates the changes during just the first year (2013 to 2014). The change maps are shown with a stretched red-blue color scheme in which solid red represents areas that have aggraded substantially (i.e., by several centimeters or more) and areas of solid blue have eroded substantially. Areas of solid red and blue are not highly relevant to this study because they record migration of sand sheets (with speeds of ~10 m/yr) in and out of troughs. Areas of pale blue are the most significant because the upper portions of yardangs are generally this color, indicating small but detectable erosion of several millimeters per year in these areas. The windward sides of some yardangs have experienced substantial erosion (approximately several centimeters) in small areas (e.g., Figure 19c) that we interpret to be the result of rockfall.

Figure 20 plots the normalized frequency distribution of topographic changes for portions of the change maps with point densities of at least 10^3 returns m^{-2}. The most common value of topographic change (i.e., the peak of the distribution) is 7 mm for the 2 year period between October 2013 and October 2015. This value is close to the sum of the most common change values for 2013 to 2014 (3 mm) and 2014 to 2015 (4 mm). These values are similar to the long-term erosion rate (3–4 mm/yr for the past ~10^6 years; (section 1.2.1). We also calculated frequency distributions of topographic changes from just those areas within 1 m from the base of the yardangs and/or in areas of steep slopes and/or in areas of large negative curvatures in an attempt to determine whether there are detectable spatial variations in erosion rates as a function of topographic factors. These alternative distributions were all very similar to those plotted in Figure 20. This result is consistent with the relatively uniform patterns of erosion illustrated by an approximately uniform pale blue color on both the windward and lee sides of most of the yardangs. This

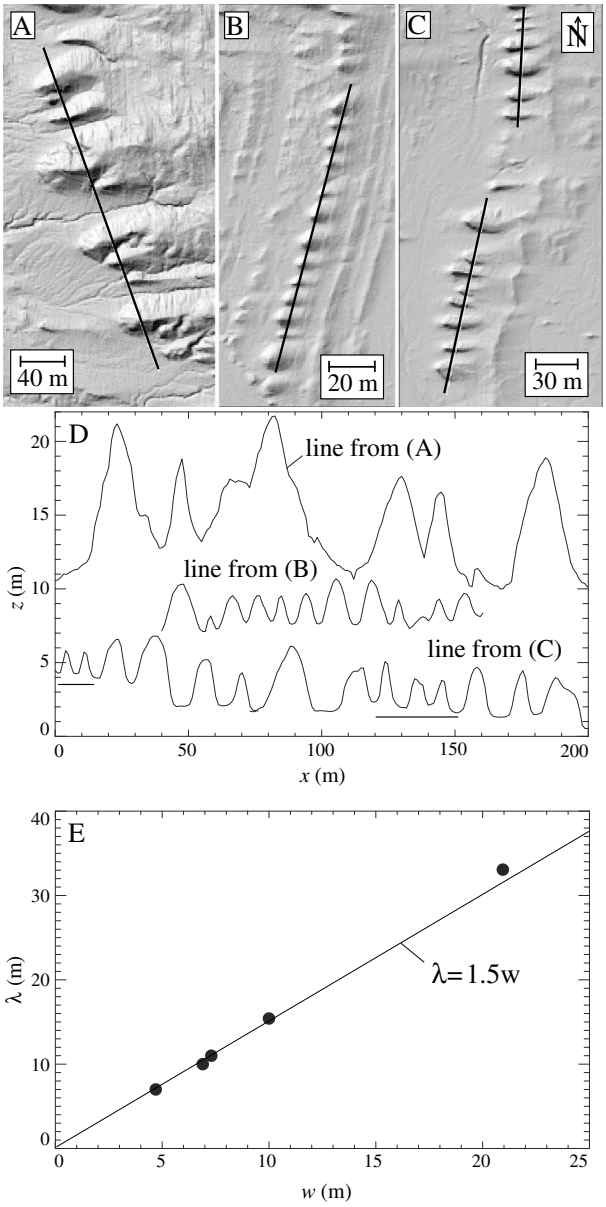

Figure 17. Plots illustrating the linear relationship between mean yardang spacing and width. (a–c) Shaded-relief images of the three rows of yardangs chosen for analysis. (d) Plots of the topographic cross sections indicated in (a–c). The two lines shown below the lowest plot indicate where subsets of the cross section were considered in order to maximize the range of spatial scales captured by the analysis. (e) Plot of mean yardang spacing versus width extracted from the profiles plotted in (d).

uniformity suggests that yardangs have evolved their shapes so that erosion rates on the front of the yardangs and in the troughs (where abrasion is dominant) are similar to those on the tops and lee sides (where water-driven processes are important and may be dominant).

4. Discussion

4.1. The Role of Substrate Heterogeneity and Controls on Yardang Aspect Ratio

The results of this paper demonstrate the important roles exerted by substrate heterogeneity on yardang development and morphology in OWSVRA. Yardang development can be enhanced by substrate heterogeneity, as evidenced by the fact that yardangs in OWSVRA form primarily in the stratigraphic unit with the most heterogeneity in mechanical strength, that is, the Borrego Formation. In the absence of heterogeneity, the instability of yardang formation (in which wind and wind-blown sediment are focused into incipient troughs) may not be initiated fast enough for the stabilizing effect of hillslope diffusion to be overcome. Substrate heterogeneity controls where yardangs tend to develop, that is, along rows where resistant strata are exposed on the windward sides of yardangs. The strikes and dips of bedrock strata exert a first-order control on yardang morphology, especially yardang aspect ratios. The numerical model of the companion paper (Pelletier, 2018) provides a theoretical basis for these conclusions. One possible implication of the role of substrate heterogeneity on yardang development is that yardang fields may not necessarily end in demise, as proposed by Barchyn and Hugenholtz (2015). As long as the substrate is heterogeneous, yardangs may continue to develop as resistant beds are exhumed.

It is important to distinguish among yardangs that form mainly parallel to versus those that form mainly perpendicular to bedding strike. When yardangs form nearly parallel to strike, variations in rock strength among layers is the primary driver of the yardang instability as weaker strata erode faster, creating accommodation space for more wind and sand resulting in higher erosion rates in a positive feedback. When yardangs form more nearly perpendicular to strike, topographic variations generated by variations in rock strength among strata are oriented primarily perpendicular to the wind direction. In these cases, the yardang-forming instability may be triggered by small-scale variations in erodibility (e.g., joints and other local weaknesses with a bed) and/or by preexisting topography.

The fact that bedrock structure influences the morphology of yardangs suggests that the thickness and/or compressive strength of resistant units exposed in individual yardangs should correlate with the height/widths of those yardangs. At present we do not have enough Schmidt Hammer measurements that are sufficiently well distributed among different yardangs in the study area to test for such a correlation. Such a test is an important future research need in this and other yardang fields where structure plays an important role in yardang development.

Figure 14 demonstrates that yardangs with an aspect ratio close to 4 are rare in OWSVRA. Instead, aspect ratios are predominantly a function of bedrock structure, with typical values of 1–3 when strata are steeply dipping and strike perpendicular to the wind direction and greater than 5 when strata strike subparallel to the wind direction. These results suggest that the concept model of Ward and Greeley (1984) that yardangs evolve to an ideal aspect ratio of 4 does not apply to the OWSVRA yardangs. The companion paper

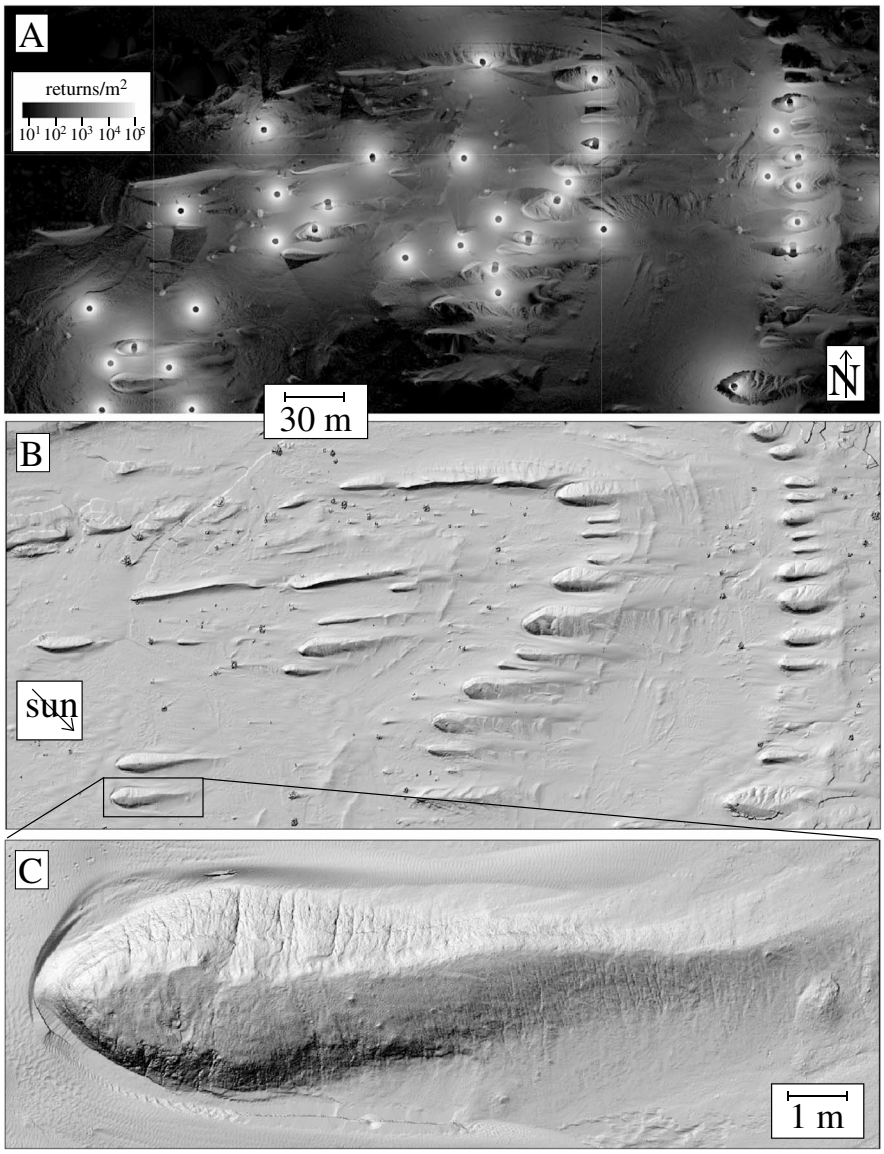

Figure 18. Maps illustrating the layout and results of the multitemporal TLS surveys. (a) Gray scale plot of the density of returns. (b) Shaded-relief image of the bare-earth DEM produced by the surveys. (c) Close-up of one of the yardangs, illustrating the details provided.

(Pelletier, 2018) examines this issue more closely from a theoretical perspective and concludes that the yardangs with an aspect ratio of 4 do not minimize drag.

4.2. Spatial Variations in Sediment Fluxes Around Yardangs

The data presented in Figure *8* demonstrate the sensitivity of eolian sediment fluxes to topographic position around yardangs. The data demonstrate that eolian sediment fluxes increase systematically with the degree of topographic convergence in the trough. The four highest eolian sediment fluxes were measured perpendicular to the widest portion of the yardangs. Among these locations, eolian sediment fluxes were higher closer to yardangs (locations 3 and 4) compared to locations farther from yardangs (locations 2 and 5). Also, there was higher eolian sediment flux of on the side where an adjacent yardang was present (locations 2 and 3) compared to sides where it was not (locations 4 and 5). These results highlight the sensitivity of flux, and by inference abrasion rate, to the degree of flow convergence/divergence around yardangs, with eolian sediment fluxes increasing by up to a factor of three in locations of strong convergence and decreasing by up to a factor of 3 (relative to the upstream sediment flux) in areas of flow divergence.

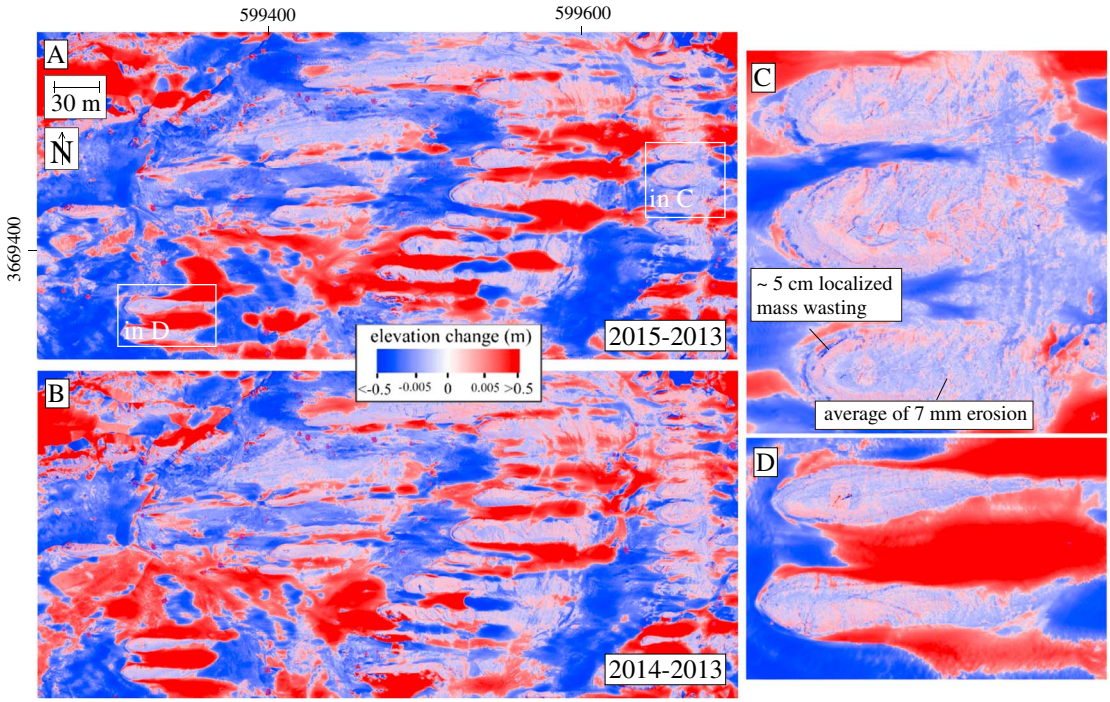

Figure 19. Color map of elevation changes measured from (a) October 2013 to 2015 and (b) October 2013 to 2014. (c and d) Close-up providing detail of change to individual yardangs.

4.3. Yardangs as Asymmetric Gaussians

Figure 12 demonstrates that asymmetric Gaussians represent the first-order morphology of yardangs. We caution that equation (2) may not be the best or only mathematical function that represents yardangs. Future work should carefully evaluate the relative efficacy of alternative functions to the asymmetric Gaussian. One drawback of equation (2) is that it may not represent the pointedness (in map view) or near-verticality of slopes of the windward side of yardangs adequately. In map view, the windward sides of yardangs appear to be more parabolic in shape compared to the asymmetric Gaussians in Figure 12b. However, an important characteristic of a Gaussian is the presence of a concave zone on the lower portions.

Other functions, such as parabolas, that might fit the upper portions of yardangs well do not include such concave zones.

4.4. Comparison of Sediment Flux Profile to Results Reported in the Literature

Studies have demonstrated the applicability of both exponential and power law relationships to data for vertical eolian sediment flux profiles (Dong et al., 2006). The data we collected from ≈0.1 to 1 m above the ground are consistent with an advection-diffusion-settling model with transport near saltation-suspension threshold, that is, with a Rouse number of approximately 2.5. Although this conclusion is specific to this range of heights above the ground, this range is the approximate rate of heights where the abrasion of a vertical rod has been observed to be a maximum (e.g., Sharp, 1964,1980). The fact that Eolian sediments are transported near the saltation-suspension threshold result is consistent with the relatively fine-grained nature of bed sediment in the study site. The median grain diameter at 0.1 to 1 m above the ground was found to be ≈80–120 μm (Figure 11), that is, small enough to be in modified saltation or short-term suspension when u_* exceeds 0.4 m/s for the smaller end of median grain sizes and when u_* exceeds 0.7 m/s for the larger end of median grain sizes (Figure 8 of Újvári et al., 2016).

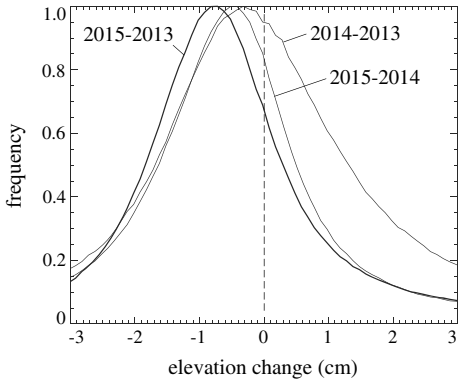

Figure 20. Frequency distributions (normalized so that most frequent change is 1) of topographic changes measured in the multitemporal TLS surveys.

These shear velocities are close to or within the range of geomorphically most effective shear velocities for the study site.

4.5. Erosion Rates as Inferred From Multitemporal TLS

The results of the multitemporal TLS surveys suggest that yardang erosion is more uniform than one might expect based on the fact that abrasion is localized on the windward sides of yardangs and in the troughs among yardangs. The maps of topographic change demonstrate, together with pervasive rill development observed in the field, that water-driven erosional processes, perhaps acting in concert with eolian deflation, are able to keep pace with eolian abrasion focused in troughs such that erosion rate appears to be relatively uniform despite large differences in slope gradient between yardangs and troughs.

4.6. Comparison to Results From the Qaidam Basin and Implications for Other Yardang Fields

Recent interest in the yardangs of the Qaidam Basin of northwestern China (e.g., Hu et al., 2017; Kapp et al., 2011; Li et al., 2016; Rohrmann et al., 2013) provides an opportunity to compare and contrast our results with those of another well-studied yardang field. Hu et al. (2017) measured 16,749 yardangs in this basin and documented that yardangs exposed along the windward limbs of anticlines have a lower average length-to-width ratio than those exposed along the leeward limbs, a result they attributed different angles between the wind direction and bedding strike as well as the presence of interbedded strata with variable erosional resistance. Our results complement those of Hu et al. (2017) by providing quantitative relationships among yardang aspect ratios and the strikes and dips of underlying strata.

Water-driven erosional processes act as an important limiter of yardang height in OWSVRA. Our conclusion that water-driven erosional processes are essential in yardang evolution at OWSVRA is consistent with the conclusions of prior studies (e.g., Brookes, 2001, 2003; Dong et al., 2012). This result suggests that yardangs can be expected to be steeper, all else being equal, in more arid regions where water-driven erosional processes are less efficient and hence where yardang height may only be limited by mass wasting. Indeed, the steepest yardangs on Earth are generally associated with the Lut Desert (Ehsani & Friedrich, 2008) and the arid regions of northwestern China including the Qaidam and Hami Basins (Pullen et al., 2017). More quantitative tests of the association between climate and yardang morphology are needed.

Structural cross-section data and cosmogenic radionuclide data allow eolian erosion rates to be estimated for the Qaidam Basin at different time scales, similar to the erosion rate estimates of this paper for OWSVRA. Erosion rates measured over time scales of thousands of years (from cosmogenic radionuclides) and millions of years (from geological cross sections) are in excess of 0.3 mm/yr in the Qaidam (Kapp et al., 2011; Rohrmann et al., 2013). These rates are somewhat lower than the rates documented here for OWSVRA. Both study sites, however, highlight the fact that high erosion rates can occur in eolian environments even with negligible large-scale relief. In areas with limited vegetation cover, relatively erodible rock, and a steady supply of abrasive sediments, an eolian buzzaw analogous to the glacial buzzsaw (e.g., Whipple et al., 1999) can act to maintain low large-scale relief despite high rock uplift rates. Both the Qaidam Basin and OWSVRA appear to be examples of such a buzzsaw in action.

5. Conclusions

We documented a previously undescribed set of yardang in Ocotillo Wells SVRA in California. Field observations at OWSVRA indicate that bedrock structure and noneolian processes play substantial roles in controlling yardang morphology. We presented measurement data quantifying (1) substrate heterogeneity/structure, (2) the spatial variability (horizontally and vertically) of eolian sediment fluxes, (3) erosion rates, and (4) measurements of yardang shape and extents (length, width, and height). We found that yardangs in OWSVRA are well characterized as asymmetric Gaussian functions. Yardang aspect ratios correlate strongly with bedrock structural attributes, specifically with the tangent of the dip and the strike relative to the prevailing wind direction. Yardang spacing is proportional to width. Yardangs at OWSVRA are not self-similar in height: height increases as the square root of width such that larger yardangs have lower slope gradients, a result we suggest may be due to the more resistant beds associated with taller yardangs. Sediment fluxes are a maximum in the troughs between yardangs, consistent with the hypothesis that yardang development involves the focusing of wind and wind-blown sediment into troughs. The vertical distribution of eolian sediment flux follows a power law with an exponent of -2.5, consistent with an advection-diffusion-settling model for eolian

transport near the transition between saltation and suspension. Erosion rates measured by multitemporal TLS surveys are several mm/yr and comparable to erosion rates estimated over time scales of ~10^6 years using geologic constraints.

Acknowledgments
I wish to thank Giovanni Coco, Tom Barchyn, Doug Sherman, and an anonymous reviewer for comments that significantly improved the manuscript. This study was supported by NSF award EAR-1323148. We thank the staff of Ocotillo Wells SVRA for permission to conduct field work in the park and for logistical support. We thank Michael Holt for assistance fabricating the MWAC towers. We thank Mike Himmerich of Borrego Springs, California, for maintaining CWOP station DW1021 and for helping us locate a long-term archive of the wind data from his station.

References

Al-Dousari, A. M., Al-Elaj, M., Al-Enezi, E., & Al-Shareeda, A. (2009). Origin and characteristics of yardangs in the Um Al-Rimam depressions (N Kuwait). *Geomorphology*, *104*(3-4), 93–104. https://doi.org/10.1016/j.geomorph.2008.05.010

Anderson, R. S. (1986). Erosion profiles due to particles entrained by wind: Application of an eolian sediment transport model. *Geological Society of America Bulletin*, *97*(10), 1270–1278. https://doi.org/10.1130/0016-7606(1986)97%3C1270:EPDTPE%3E2.0

Anderson, R. S., & Hallet, B. (1986). Sediment transport by wind: Toward a general model. *Geological Society of America Bulletin*, *97*(5), 523–523. https://doi.org/10.1130/0016-7606(1986)97%3C523:STBWTA%3E2.0.CO;2

Barchyn, T. E., & Hugenholtz, C. H. (2015). Yardang evolution from maturity to demise. *Geophysical Research Letters*, *42*, 5865–5871. https://doi.org/10.1002/2015GL064477

Blackwelder, E. (1934). Yardangs. *Geological Society of America Bulletin*, *45*(1), 159–166. https://doi.org/10.1130/GSAB-45-159

Bosworth, T. O. (1922). *Geology of the Tertiary and Quaternary periods in the north-west part of Peru*. London: Macmillan and Company.

Breed, C. S., McCauley, J. F., & Whitney, M. J. (1989). Wind erosion forms. In D. S. G. Thomas (Ed.), *Arid zone geomorphology* (pp. 284–307). New York: Halstead Press.

Brookes, I. A. (2001). Aeolian erosional lineations in the Libyan Desert, Dakhla Region, Egypt. *Geomorphology*, *39*(3-4), 189–209. https://doi.org/10.1016/S0169-555X(01)00026-5

Brookes, I. A. (2003). Palaeofluvial estimates from exhumed meander scrolls, Taref Formation (Turonian), Dakhla Region, Western Desert, Egypt. *Cretaceous Research*, *24*(2), 97–104. https://doi.org/10.1016/S0195-6671(03)00033-8

Charnock, H. (1955). Wind stress on a water surface. *Quarterly Journal of the Royal Meteorological Society*, *81*(350), 639–640. https://doi.org/10.1002/qj.49708135027

Culling, W. E. H. (1960). Analytical theory of erosion. *Journal of Geology*, *68*(3), 336–344. https://doi.org/10.1086/626663

Dong, Z., Lv, P., Lu, J., Qian, G., Zhang, Z., & Luo, W. (2012). Geomorphology and origin of yardangs in the Kumtagh Desert, Northwest China. *Geomorphology*, *139-140*, 145–154. https://doi.org/10.1016/j.geomorph.2011.10.012

Dong, Z., Qian, G., Luo, W., & Wang, H. (2006). Analysis of the mass flux profiles of an aeolian saltating cloud. *Journal of Geophysical Research*, *111*, D16111. https://doi.org/10.1029/2005JD006630

Dorsey, R. J., Housen, B. A., Janecke, S. U., Fanning, C. M., & Spears, A. L. F. (2011). Stratigraphic record of basin development within the San Andreas fault system: Late Cenozoic Fish creek-Vallecito basin, southern California. *Geological Society of America Bulletin*, *123*(5-6), 771–793. https://doi.org/10.1130/B30168.1

Dunne, T., Malmon, D. V., & Mudd, S. M. (2010). A rain splash transport equation assimilating field and laboratory measurements. *Journal of Geophysical Research*, *115*, F01001. https://doi.org/10.1029/2009JF001302

Ehsani, A. H., & Friedrich, Q. F. (2008). Application of self organizing map and SRTM data to characterize yardangs in the Lut Desert, Iran. *Remote Sensing of Environment*, *112*(7), 3284–3294. https://doi.org/10.1016/j.rse.2008.04.007

El-Baz, F., Breed, C. S., Grolier, M. J., & McCauley, J. F. (1979). Eolian features in the western desert of Egypt and some applications to Mars. *Journal of Geophysical Research*, *84*(B14), 8205–8221. https://doi.org/10.1029/JB084iB14p08205

Farrell, E. J. (2012). Characterizing vertical mass flux profiles in aeolian saltation systems, (PhD dissertation). Retrieved from http://oaktrust.library.tamu.edu/handle/1969.1/ETD-TAMU-2012-05-10862. College Station, TX: Texas A&M University.

Furbish, D. J., Haff, P. K., Dietrich, W. E., & Heimsath, A. M. (2009). Statistical description of slope-dependent soil transport and the diffusion-like coefficient. *Journal of Geophysical Research*, *114*, F00A05. https://doi.org/10.1029/2009JF001267

Goudie, A., Stokes, S., Cook, J., Samieh, S., & El-Rashidi, O. A. (1999). Yardang landforms from Kharga Oasis, south-western Egypt. *Zeitschrift für Geomorphologie Supplementband*, *116*, 97–112.

Greeley, R., Bender, K., Thomas, P. E., Schubert, G., Limonadi, D., & Weitz, C. M. (1995). Wind-related features and processes on Venus: Summary of Magellan results. *Icarus*, *115*(2), 399–420. https://doi.org/10.1006/icar.1995.1107

Greeley, R., & Iversen, J. D. (1985). *Wind as a geological process on Earth, Mars, Venus and Titan*. New York: Cambridge University Press. https://doi.org/10.1017/CBO9780511573071

Halimov, M., & Fezer, F. (1989). Eight yardang types in Central Asia. *Zeitschrift für Geomorphologie*, *33*, 205–217.

Hanks, T. C. (2000). The age of scarplike landforms from diffusion-equation analysis. In J. S. Noller, J. M. Sowers, & W. R. Lettis (Eds.), *Quaternary geochronology: Methods and applications* (pp. 313–338). Washington, DC: American Geophysical Union. https://doi.org/10.1029/RF004p0313

Hedin, S. (1905). Lop Nor: Scientific results of a journey in central Asia (1889–1902), v. 2, Stockholm.

Hodge, R., Brasington, J., & Richards, K. (2009). In situ characterization of grain-scale fluvial morphology using Terrestrial Laser Scanning. *Earth Surface Processes and Landforms*, *34*(7), 954–968. https://doi.org/10.1002/esp.1780

Hörner, N. G. (1932). Lop Nor: Topographic and geological summary. *Geografiska Annaler*, *14*, 297–321.

Housen, B. A., & Dorsey, R. J. (2010). Magnetostratigraphy and paleomagnetism of the Plio-Pleistocene Arroyo Diablo and Borrego Formations in the Borrego Badlands, western Salton Trough. CA. *Eos, Transactions, American Geophysical Union*, GP23C-8.

Hu, C., Chen, N., Kapp, P., Chen, J., Xiao, A., & Zhao, Y. (2017). Yardang geometries in the Qaidam Basin and their controlling factors. *Geomorphology*, *299*, 142–151. https://doi.org/10.1016/j.geomorph.2017.09.029

Janecke, S. U., Dorsey, R. J., Steely, A. N., Kirby, S. M., Lutz, A. T., Housen, B. A., et al. (2010). High geologic slip rates since early Pleistocene initiation of the San Jacinto and San Felipe fault zones in the San Andreas fault system: Southern California, USA. *Geological Society of America Special Papers*, *475*, 1–48. https://doi.org/10.1130/2010.2475

Kapp, P., Pelletier, J. D., Rohrmann, A., Heermance, R., Russell, J., & Ding, L. (2011). Wind erosion in the Qaidam basin, central Asia: Implications for tectonics, paleoclimate, and the source of the Loess plateau. *GSA Today*, *21*(4), 4–10. https://doi.org/10.1130/GSATG99A.1

Kirby, S. M., Janecke, S. U., Dorsey, R. J., Housen, B. A., Langenheim, V., McDougall, K., & Steely, A. N. (2007). Pleistocene Brawley and Ocotillo formations: Evidence for initial strike-slip deformation along the San Felipe and San Jacinto fault zones, southern California. *Journal of Geology*, *115*(1), 43–62. https://doi.org/10.1086/509248

Komar, P. D. (1983). Shape of streamlined islands on Earth and Mars: Experiments and analyses of the minimum drag form. *Geology*, *11*(11), 651–654. https://doi.org/10.1130/0091-7613(1983)11%3C651:SOSIOE%3E2.0.CO;2

Komar, P. D. (1984). The lemniscate loop—Comparisons with the shapes of streamlined landforms. *Journal of Geology*, *92*(2), 133–145. https://doi.org/10.1086/628844

Krinsley, D. B. (1970). A geomorphological and palaeoclimatological study of the playas of Iran, U.S. Geological Survey Final Report, Contract PRO CP, 70–800.

Laity, J. E. (2011). Wind erosion in drylands. In D. S. G. Thomas (Ed.), *Arid zone geomorphology: Process, form and change in drylands* (Chap. 21, 3rd ed., pp. 539–568). Chichester, UK: John Wiley. https://doi.org/10.1002/9780470710777.ch21

Laity, J. E., & Bridges, N. T. (2009). Ventifacts on Earth and Mars: Analytical, field, and laboratory studies supporting sand abrasion and windward feature development. *Geomorphology*, *105*(3-4), 202–217. https://doi.org/10.1016/j.geomorph.2008.09.014

Li, J., Dong, Z., Qian, G., Zhang, Z., Luo, W., Lu, J., & Wang, M. (2016). Yardangs in the Qaidam Basin, northwestern China: Distribution and morphology. *Aeolian Research*, *20*, 89–99. https://doi.org/10.1016/j.aeolia.2015.11.002

Liu, X., Zhang, Z., & Peterson, J. (2009). Evaluation of the performance of DEM interpolation algorithms for LiDAR data. In *2009 Surveying and Spatial Sciences Institute Biennial International Conference (SSC 2009): Spatial Diversity, 28 Sep - 2 Oct 2009*. Adelaide, Australia: Digital Document. Retrieved from https://eprints.usq.edu.au/6476/

Lutz, A. T., Dorsey, R. J., Housen, B. A., & Janecke, S. U. (2006). Stratigraphic record of Pleistocene faulting and basin evolution in the Borrego Badlands, San Jacinto fault zone, Southern California. *Geological Society of America Bulletin*, *118*(11/12), 1377–1397. https://doi.org/10.1130/B25946.1

Mandt, K. E., de Silva, S. L., Zimbelman, J. R., & Crown, D. A. (2008). Origin of the Medusae Fossae Formation, Mars: Insights from a synoptic approach. *Journal of Geophysical Research*, *113*, E12011. https://doi.org/10.1029/2008JE003076

Martin, R. L., & Kok, J. F. (2017). Wind-invariant saltation height implies linear scaling of aeolian saltation flux with shear stress. *Science Advances*, *3*(6), e1602569. https://doi.org/10.1126/sciadv.1602569

McCauley, J. F., Grolier, M. J., & Breed, C. S. (1977). Yardangs. In D. O. Doehring (Ed.), *Geomorphology in arid regions. Proceedings, 8th Annual Geomorphology Symposium* (pp. 233–272). Binghamton, New York: Publication in Geomorphology.

McCool, D. K., Foster, G. R., Mutchler, C. K., & Meyer, L. D. (1989). Revised slope length factor for the Universal Soil Loss Equation. *Transactions of the American Society of Agricultural Engineers*, *32*(5), 1571–1576. https://doi.org/10.13031/2013.31192

McKean, J., Dietrich, W. E., Finkel, R. C., Southon, J. R., & Caffee, M. W. (1993). Quantification of soil production and downslope creep rates from cosmogenic ^{10}Be accumulations on a hillslope profile. *Geology*, *21*(4), 343–346. https://doi.org/10.1130/0091-7613(1993)021%3C0343:QOSPAD%3E2.3.CO;2

Nearing, M. (1997). A single, continuous function for slope steepness influence on soil loss. *Soil Science Society of America Journal*, *61*(3), 917–919. https://doi.org/10.2136/sssaj1997.03615995006100030029x

Pelletier, J. D. (2012). A spatially distributed model for the long-term suspended sediment discharge and delivery ratio of drainage basins. *Journal of Geophysical Research*, *117*, F02028. https://doi.org/10.1029/2011JF002129

Pelletier, J. D. (2013). Deviations from self-similarity in barchan form and flux: The case of the Salton Sea dunes, California. *Journal of Geophysical Research: Earth Surface*, *118*, 2406–2420. https://doi.org/10.1002/2013JF00286

Pelletier, J. D. (2018). Controls on yardang development and morphology: 2. Numerical modeling. *Journal of Geophysical Research: Earth Surface*, *123*. https://doi.org/10.1012/2017JF004462

Pullen, A., Kapp, P., & Chen, N. (2017). Development of stratigraphically controlled, eolian-modified unconsolidated gravel surfaces and yardang fields in the wind-eroded Hami Basin, northwestern China. *Geological Society of America Bulletin*, *130*(3-4), 630–648. https://doi.org/10.1130/B31734.1

Rasmussen, K. R., & Sørensen, M. (2008). Vertical variation of particle speed and flux density in aeolian saltation: Measurement and modeling. *Journal of Geophysical Research*, *113*, F02S12. https://doi.org/10.1029/2007JF000774

Raupach, M. R. (1991). Saltation layers, vegetation canopies and roughness lengths. In O. E. Barndorff-Nielsen & B. B. Willetts (Eds.), *Aeolian grain transport 1*, *Acta Mechanica Supplementum* (Vol. 1, pp. 83–96). Vienna: Springer. https://doi.org/10.1007/978-3-7091-6706-9_5

Rohrmann, A., Heermance, R., Kapp, P., & Cai, F. (2013). Wind as the primary driver of erosion in the Qaidam Basin, China. *Earth and Planetary Science Letters*, *374*, 1–10. https://doi.org/10.1016/j.epsl.2013.03.011

Sharp, R. P. (1964). Wind-driven sand in the Coachella Valley, California. *Geological Society of America Bulletin*, *75*(9), 785–804. https://doi.org/10.1130/0016-7606(1964)75%5B785:WSICVC%5D2.0.CO;2

Sharp, R. P. (1980). Wind-driven sand in the Coachella Valley, California: Further data. *Geological Society of America Bulletin*, *91*(12), 724–730. https://doi.org/10.1130/0016-7606(1980)91%3C724:WSICVC%3E2.0.CO;2

Sherman, D. J. (1992). An equilibrium relationship for shear velocity and apparent roughness length in aeolian saltation. *Geomorphology*, *5*(3-5), 419–431. https://doi.org/10.1016/0169-555X(92)90016-H

Sherman, D. J., & Farrell, E. J. (2008). Aerodynamic roughness lengths over movable beds: Comparison of wind tunnel and field data. *Journal of Geophysical Research*, *113*, F02S08. https://doi.org/10.1029/2007JF000784

De Silva, S. L., Bailey, J. E., Mandt, K. E., & Viramonte, J. M. (2010). Yardangs in terrestrial ignimbrites: Synergistic remote and field observations on Earth with applications to Mars. *Planetary and Space Science*, *58*(4), 459–471. https://doi.org/10.1016/j.pss.2009.10.002

Sundborg, A. (1955). Meteorological and climatological conditions for the genesis of aeolian sediment. *Geografiska Annaler*, *37*, 94–111.

Újvári, G., Kok, J. F., Varga, G., & Kovács, J. (2016). The physics of wind-blown loess: Implications for grain size proxy interpretations in Quaternary paleoclimate studies. *Earth-Science Reviews*, *154*, 247–278. https://doi.org/10.1016/j.earscirev.2016.01.006

United States Department of Agriculture-Agricultural Research Service (2014). Revised Universal Soil Loss Equation (RUSLE) - Welcome to RUSLE 1 and RUSLE 2. Digital document. Retrieved from https://www.ars.usda.gov/southeast-area/oxford-ms/national-sedimentation-laboratory/watershed-physical-processes-research/docs/revised-universal-soil-loss-equation-rusle-welcome-to-rusle-1-and-rusle-2/

University of Utah (2016). Meso West, digital data. Retrieved from http://mesowest.utah.edu/cgi-bin/droman/download_ndb.cgi?stn=d1021, last accessed July 21, 2016

Ward, A. W. (1979). Yardangs on Mars: Evidence of recent wind erosion. *Journal of Geophysical Research*, *84*(B14), 8147–8166. https://doi.org/10.1029/JB084iB14p08147

Ward, A. W., & Greeley, R. (1984). Evolution of the yardangs at Rogers Lake, California. *Geological Society of America Bulletin*, *95*(7), 829–837. https://doi.org/10.1130/0016-7606(1984)95%3C829:EOTYAR%3E2.0.CO;2

Waters, M. R. (1983). Late Holocene lacustrine chronology and archaeology of ancient Lake Cahuilla, California. *Quaternary Research*, *19*(03), 373–387. https://doi.org/10.1016/0033-5894(83)90042-X

Western Regional Climate Center (WRCC) (2016a). Digital data. Retrieved from http://www.wrcc.dri.edu/cgi-bin/cliMAIN.pl?ca6383, last accessed July 21, 2016

Western Regional Climate Center (WRCC) (2016b). Digital data. Retrieved from http://www.wrcc.dri.edu/cgi-bin/wea_windrose.pl?caZSSWE, last accessed July 21, 2016

Western Regional Climate Center (WRCC) (2016c). Digital data. Retrieved from http://www.wrcc.dri.edu/cgi-bin/wea_windrose.pl?caZSSW, last accessed July 21, 2016

Whipple, K. X., Kirby, E., & Brocklehurst, S. H. (1999). Geomorphic limits to climate-induced increases in topographic relief. *Nature*, *401*(6748), 39–43. https://doi.org/10.1038/43375

Wilson, S. J., & Cooke, R. U. (1980). Wind erosion. In M. J. Kirkby & P. P. C. Morgan (Eds.), *Soil erosion* (pp. 217–251). Chichester, UK: John Wiley.

Witte, L. P., & Backstrom, J. E. (1951). Some properties affecting the abrasion resistance of air-entrained concrete. *Proceedings-American Society for Testing and Materials*, *51*, 1141–1155.